

The skating of drops impacting over gas or vapour layers

P. García-Geijo¹, G. Riboux¹ and J.M. Gordillo^{1,†}

¹Área de Mecánica de Fluidos, Departamento de Ingeniería Aeroespacial y Mecánica de Fluidos, Universidad de Sevilla, Avenida de los Descubrimientos s/n, 41092 Sevilla, Spain

(Received 12 June 2023; revised 22 December 2023; accepted 30 December 2023)

We report numerical simulations confirming the predictions in Gordillo & Riboux (*J. Fluid Mech.*, vol. 941, 2022, A10), where we elucidated the lubrication mechanism by which a drop of a low-viscosity liquid impacting over a smooth solid substrate skates over a thin gas film that prevents contact with the wall. Moreover, with the purpose of explaining the so-called lift-off mechanism reported in Kolinski *et al.* (*Phys. Rev. Lett.*, vol. 112, issue 13, 2014, 134501), we extend our previous findings and derive expressions for the time-varying thickness of the gas layer at the region where the distance to the wall is minimum, finding good agreement with the numerical results. In addition, we report that our predictions for the minimum thickness of the gas film separating a falling drop from a wall at room temperature follow closely the experimental values when gas kinetic effects are retained in the analysis, and also report that the analogous equation for the minimum thickness of the vapour layer formed after a drop impacts a superheated wall predicts well the experimental measurements.

Key words: boiling, drops

1. Introduction

The impact of a drop over a substrate has been the subject of intense research efforts during the past decades as a consequence of its relevance in a myriad of natural and technological processes; see e.g. Josserand & Thoroddsen (2016). One of the many open questions that remains to be solved and has received substantial attention in recent years refers to the description and quantification of the conditions under which a drop impacting a superheated substrate skates over a vapour film, a phenomenon referred to as the dynamic

† Email address for correspondence: jgordill@us.es

Leidenfrost effect, which limits the cooling rate of solids in heat transfer technological applications (Tran *et al.* 2012, 2013; Shirota *et al.* 2016). Indeed, as a consequence of the smallness of the thermal conductivity of gases, the existence of a stable vapour film beneath the drop reduces the heat flux and therefore the cooling capacity of the liquid (van Limbeek *et al.* 2017).

The theoretical and numerical studies aimed at describing the effect of a gas or vapour layer on the impact of a drop over a solid substrate were pioneered by Smith, Li & Wu (2003) and Korobkin, Ellis & Smith (2008), who coupled the equations for the inviscid motion of a two-dimensional drop impacting either a wall or a thin liquid layer with the lubrication equations for the gas. Later, Mandre, Mani & Brenner (2009), Mani, Mandre & Brenner (2010) and Mandre & Brenner (2012) made use of the theoretical and numerical framework already introduced by Smith *et al.* (2003) and Korobkin *et al.* (2008) with the purpose of deriving scaling relationships for the dimple height – namely, the thickness of the pancake-shaped bubble entrapped at the centre of the impacting drop – and also for the minimum distance between the drop and the wall, which is attained not at the axis of symmetry, but at an off-centre position. The scaling for the dimple height deduced by Mandre *et al.* (2009) in the two-dimensional case and by Hicks & Purvis (2010) for the more realistic case of spherical drops was confirmed via experiments and also via numerical simulations by Bouwhuis *et al.* (2012) who, in addition, discovered a new regime dominated by capillarity that describes the entrapment of bubbles at low impact velocities. Let us point out here that the analysis of the entrapment of a gas pocket beneath a falling liquid mass is analogous to the cushioning effect of the air entrapped after a solid impacts a free surface, a physical situation that has been analysed by e.g. Wilson (1989), Ross & Hicks (2019) and Moore (2021), using Wagner’s original ideas (Wagner 1932). Again, back in the context of drops falling over a wall, Duchemin & Josserand (2011) developed a boundary integral method coupled with simplified lubrication equations for the gas flow, and reported numerical results for the minimum film thickness that did not follow the predictions in Mandre *et al.* (2009), Mani *et al.* (2010) and Mandre & Brenner (2012).

From the purely experimental point of view, and making use of high-speed imaging techniques, Chandra & Avedisian (1991) and Thoroddsen *et al.* (2005) were the first to report the shape and thickness of the bubble entrapped at the centre of the drop, whereas Kolinski, Mahadevan & Rubinstein (2014*b*) reported experimental data on the time-varying minimum film thickness, and described what they called the lift-off mechanism, which takes place when a drop skates over a nanometric gas film, finding that this effect depends on the gas to liquid viscosity ratio. Very recently, Chantelot & Lohse (2021, 2023) extended the previous experimental studies to the case of superheated substrates, reporting measurements of the minimum film thickness as a function of the impact velocity and of the substrate temperature, and they scaled and interpreted their own data using the ideas in Mandre *et al.* (2009) and Mandre & Brenner (2012).

Recently, Gordillo & Riboux (2022) presented a physical model based on the idea that both the liquid pressure gradient and the component of the liquid velocity along the tangent direction to the wall drive the gas flow within the spatio-temporal region where the distance between the liquid and the solid is minimum. One of the main results of Gordillo & Riboux (2022), who made extensive use of Wagner’s theoretical framework (Wagner 1932), is that the classical lubrication mechanism, by which the Couette and Poiseuille flow rates are in balance in the slightly converging geometry formed between the drop and the wall, prevents the liquid contacting the solid provided that the minimum gas layer

thickness calculated in this way is larger than the height of the substrate asperities or of the interfacial corrugations (Kim *et al.* 2011; Kolinski, Mahadevan & Rubinstein 2014a; Chantelot & Lohse 2021).

The study by Gordillo & Riboux (2022) present results that differ from those in Mandre *et al.* (2009), Mandre & Brenner (2012) and Chantelot & Lohse (2021, 2023), hence one of the main purposes in this contribution will be to decipher which of the two predictions for the minimum film thickness corresponding to the case of non-heated substrates (i.e. either the one given in Mandre *et al.* (2009), Mani *et al.* (2010) and Mandre & Brenner (2012), or the one deduced in Gordillo & Riboux (2022)) is in better agreement with numerical simulations carried out using Basilisk (Popinet 2015) in the limit in which the Knudsen number Kn defined in terms of the gas film thickness is zero, namely, when gas kinetic effects are absent (Sprittles 2024).

It could appear that the main contribution here is nothing but a confirmation of already published results, but this is not the case. Indeed, here we will also provide a quantitative explanation of the so-called lift-off mechanism first described by Kolinski *et al.* (2014b), by which the minimum thickness of the gas film increases in time after the distance to the wall has reached a minimum. In spite of several contributions in the literature on the subject, some of which are very recent (see e.g. Mishra, Rubinstein & Rycroft 2022), we have not found any physical description or theory aimed at explaining and quantifying the original observations made by Kolinski *et al.* (2014b). Then here we deduce equations for the time-dependent width of the gas layer where the liquid pressure is maximum, finding that our predictions agree with the numerical results, which – as has been pointed out in the paragraph above – have been obtained in the ideal limit in which the Knudsen number characterizing the flow in the thin gas film is zero.

This contribution also contains a comparison between our predictions and the experiments reported by de Ruiter *et al.* (2012) and Chantelot & Lohse (2023) for the case of a non-heated substrate, with such a comparison containing two fundamental differences from the analogous analysis reported in Gordillo & Riboux (2022). Indeed, the minimum film thickness is calculated here using an equation that has been validated previously by means of numerical simulations carried out in the ideal limit $Kn = 0$. But, in addition, in order to compare with experiments, we retain in the algebraic expression for the minimum film thickness the effect of Kn by replacing the actual gas viscosity with the expression for the effective gas viscosity deduced by Zhang & Law (2011). The good agreement between our predictions – which do not include any kind of adjusting parameter since the only free constant will be determined using idealized numerical simulations – and experiments indicate that, as was pointed out already by Li (2016) and Chubynsky *et al.* (2020), gas kinetic effects are essential to predict the dynamics of impacting drops that skate over a gas layer; in addition, these results provide further support to our physical description which, as it was pointed out above, differ from the one given in Mandre *et al.* (2009), Mandre & Brenner (2012) and Chantelot & Lohse (2021, 2023).

Moreover, the predictions in Gordillo & Riboux (2022) for the cases of drops impacting a superheated substrate – namely, a substrate with a temperature larger than the boiling temperature of the liquid – will be compared with the experimental data reported by Chantelot & Lohse (2021, 2023) once gas kinetic effects are taken into account through the expressions for the effective gas viscosity and the effective thermal conductivity reported by Zhang & Law (2011) and Sharipov, Cumin & Kalempa (2007), respectively.

Let us point out clearly here that it is not the purpose of this contribution to describe the contact between the liquid and the solid, i.e. the so-called touchdown problem, which

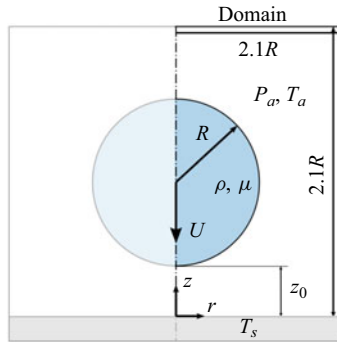


Figure 1. Sketch showing the axisymmetric domain where the numerical simulations have been carried out using Basilisk (Popinet 2015); see Appendix A for details. Here, r and z , respectively, indicate the distance to the axis of symmetry and the distance to the wall in a cylindrical coordinate system. The numerical box is a square of length $2.1R$.

remains an open question due to the fact that either the contact or the rebound of a drop impacting a solid depends on a number of factors, such as the substrate roughness, the presence of contaminants at the free interface, asymmetries, van der Waals forces, or even electrostatic effects (Kim *et al.* 2011; Kolinski *et al.* 2014a; Sprittles 2024), which lead to differences on the instant at which the gas film destabilizes under very similar experimental conditions; see e.g. Kolinski *et al.* (2014a) and de Goede *et al.* (2019). The explanation for these differences is outside the scope of this contribution, which is then focused in the description of those regimes in which a drop impacting a solid substrate, which might be heated above the boiling point of the liquid or not, skates over a thin gas film, this being a subject of recent interest in the literature (Sprittles 2024).

The manuscript is structured as follows. Section 2 is devoted to presenting the results of numerical simulations carried out using Basilisk (Popinet 2015). In § 3, we review the physical model presented in Gordillo & Riboux (2022), and compare our own predictions and those in Mandre & Brenner (2012) and Chantelot & Lohse (2023) with the numerical results. Taking into account gas kinetic effects, in § 4 we compare our predictions for the minimum gas film thicknesses with the experimental values given in de Ruiter *et al.* (2012) and Chantelot & Lohse (2023). Finally, § 5 summarizes the main results in this contribution.

2. Numerical results corresponding to the case of isothermal substrates

This section is devoted to presenting the results of simulations carried out using Basilisk (Popinet 2015) in the numerical domain depicted in figure 1, which shows a drop of radius R of a liquid with density ρ , viscosity μ , and interfacial tension coefficient σ , falling with uniform velocity U against a wall whose temperature T_s is equal to that of the gas, $T_s = T_a$ (isothermal substrate); see Appendix A for details on the numerical implementation.

Using R , R/U and ρU^2 as the characteristic values of length, time and pressure, the numerical results in this section will be expressed in terms of the Stokes and Weber numbers defined as

$$St = \frac{\rho UR}{\mu_a}, \quad We = \frac{\rho U^2 R}{\sigma}, \quad (2.1a,b)$$

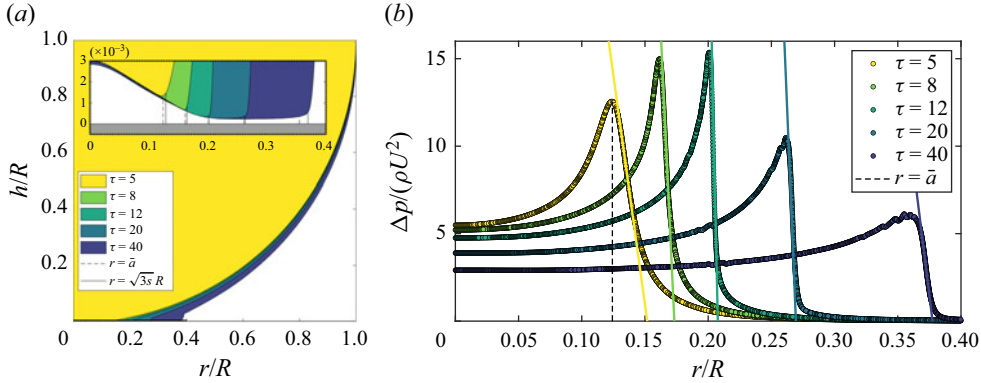


Figure 2. (a) Time-evolving shapes of a drop impacting a wall with $We = 12$ and $St = 2.6 \times 10^4$. The inset shows the geometry of both the gas pocket and the region, located at $r/R = \sqrt{3}s$ (solid line), where the drop skates over a thin gas layer. Notice that the radial position where the maximum gas pressure is attained, $r = \bar{a}$ (dashed line), verifies $\bar{a} \approx R\sqrt{3}s$. (b) Spatio-temporal evolution of the gas pressure at the wall corresponding to the values of We and St of (a). The values of $\partial p/\partial r$ at the spatio-temporal region where the gas pressure is maximum are calculated as the slopes of the solid lines in the figure.

and varied within the ranges $9 \times 10^3 \leq St \leq 4.5 \times 10^4$, $4 \leq We \leq 60$, while keeping fixed the values of the ratios $\rho_a/\rho = 10^{-3}$ and $\mu_a/\mu = 1.8 \times 10^{-2}$, with ρ_a and μ_a indicating the gas density and viscosity, respectively. For simplicity, neither compressibility nor gas kinetic effects have been retained in the numerical simulations, which, as has been pointed out above, have been carried out for the case of isothermal substrates.

The numerical results depicted in figure 2(a) reveal that as the drop approaches the wall, a dimple is formed at the axis of symmetry, entrapping a nearly cylindrical gas pocket with radius $\propto \sqrt{Rh_d}$ and thickness h_d . Figure 2 also shows that the liquid does not touch the solid but, instead, skates over a thin gas film whose minimum thickness $h_{min} \ll h_d$ is attained at $r \propto \sqrt{Rh_d}$.

The thickness of the entrapped bubble, h_d , is deduced from the mass balance (Mandre *et al.* 2009; Bouwhuis *et al.* 2012)

$$\pi U(Rh_d) \sim 2\pi\sqrt{Rh_d} \frac{h_d^3}{12\mu_a} \frac{\Delta p_d}{\sqrt{Rh_d}}, \quad (2.2)$$

where it has been taken into account that the gas flow rate per unit length induced by the pressure jump $\Delta p_d = p(r = z = 0, t) - P_a$ is $\Delta p_d \propto (h_d^3/\mu_a)(\Delta p_d/\sqrt{Rh_d})$. Since in a first approximation the liquid velocity field within the drop is irrotational, the Euler–Bernoulli equation particularized at $r = 0, z = h_d$ yields (Bouwhuis *et al.* 2012)

$$\Delta p_d \sim \rho \frac{\partial \phi}{\partial t}, \quad (2.3)$$

where $\phi \propto U\sqrt{Rh_d}$ is the value of the velocity potential at $r = 0$ created by a disk of radius $\sqrt{Rh_d}$ moving into the liquid with a velocity U ; see e.g. Peters, van der Meer & Gordillo (2013). Then since the dimple is formed in a characteristic time h_d/U , the pressure jump deduced from (2.3) reads $\Delta p_d \propto \rho U^2 \sqrt{R/h_d}$, from which, using (2.2), we obtain

$$h_d \propto RSt^{-2/3}; \quad (2.4)$$

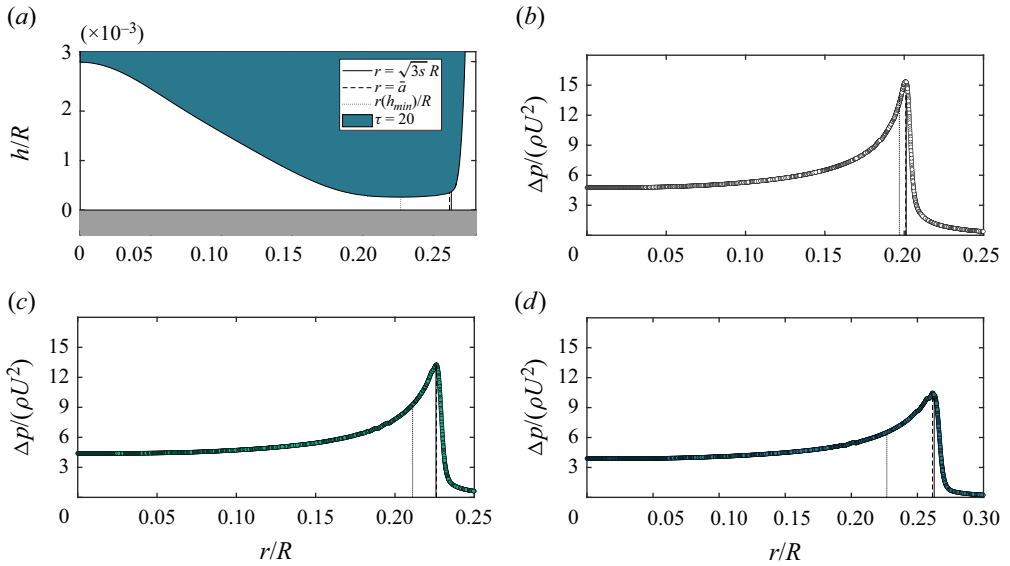


Figure 3. (a) Gas layer thickness $h(r)/R$ at $\tau = 20$ for $We = 12$ and $St = 2.6 \times 10^4$. The radial position where the minimum air film thickness is attained, $r(h_{min})/R$ (dotted vertical line), the radial position where the maximum pressure is reached, $r/R = \bar{a}/R$ (dashed vertical line), and the wetting radius, $r/R = \sqrt{3s}$ (solid vertical line), are indicated. Values of the gas pressure jump at the wall for the following instants of time: (b) $\tau = 12$, (c) $\tau = 15$, and (d) $\tau = 20$.

then the dimple is formed in a characteristic time given by

$$\Delta t_d \propto \frac{h_d}{U} \rightarrow \frac{\Delta t_d U}{R} \propto \frac{h_d}{R} \propto St^{-2/3}. \quad (2.5)$$

Hence, taking the origin of times at the instant when the drop would contact the substrate if the gas were not present, and defining the dimensionless times s and τ as

$$s = t \frac{U}{R}, \quad \tau = St^{2/3} s = St^{2/3} t \frac{U}{R}, \quad (2.6a,b)$$

the result in (2.5) indicates that the dimple is formed at the instant of time $\tau = \tau^*$, with $\tau^* \approx 12$ (Gordillo & Riboux 2022).

Figure 2(b) shows the spatio-temporal evolution of the gas pressure at the wall i.e. at $z = 0$. For a fixed value of τ , the results in figure 2(b) reveal that the gas pressure increases radially, reaching a maximum at an off-centre position that moves towards larger values of r as time progresses. In addition, figure 2 shows that the maximum gas pressure at the wall, and also the values of the local pressure gradient at the radial position where the maximum pressure is located, increase with τ , reaching a maximum at $\tau = \tau^* \approx 12$. Moreover, the results in figure 3 reveal that the maximum gas pressure and the maximum pressure gradient, calculated as the slope of the lines depicted in figure 2(b), are reached at the radial position

$$r = a(s) = R\sqrt{3s}, \quad (2.7)$$

namely, at the radius of the circular region that is wetted by a drop impacting with velocity U over a wall, a result that was checked carefully against experiments and was deduced in Riboux & Gordillo (2014) in the context of drop impact using Wagner's

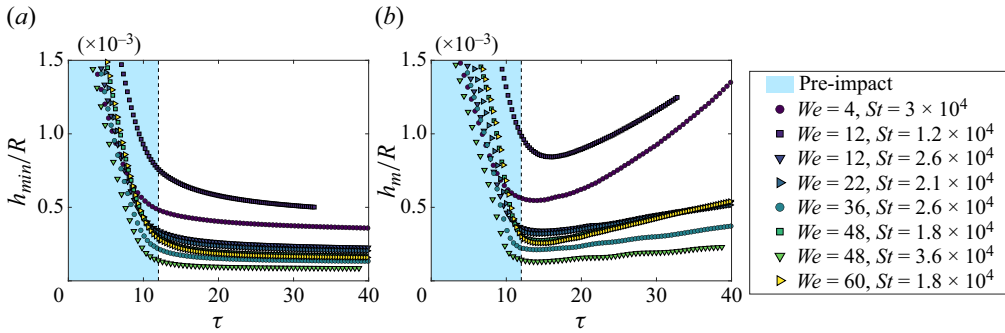


Figure 4. Time evolution of (a) the minimum gas layer thickness h_{min} , and (b) the thickness of the gas layer measured at $r/R = \sqrt{3}s$, $h_m = h(r = R\sqrt{3}s)$, corresponding to the values of We and St indicated in the legend. The pre-impact stage $\tau < 12$ is highlighted in blue.

theoretical framework (Wagner 1932). Indeed, Wagner’s theory, which has been known for nearly a century in the context of water entry problems, permits us to deduce the result in (2.7) in a quite straightforward manner; see also Wilson (1989), where (2.7) was deduced in the context of ship slamming. Readers interested in the rigorous application of Wagner’s theory (Wagner 1932) to different physical phenomena using matched asymptotic techniques are directed to Korobkin & Pukhnachov (1988), Wilson (1989), Howison, Ockendon & Wilson (1991), Scolan & Korobkin (2001), Oliver (2002), Korobkin & Scolan (2006) and Moore (2014). The results in figure 3 also suggest that in spite of the minimum gas film thickness $h_{min}(\tau)$ is not attained at the radial position where the maximum gas pressure is reached, namely, $h_m(\tau) \neq h_{min}(\tau)$, with

$$h_m(\tau) = h(r = a(s)), \tag{2.8}$$

$h_m(\tau) \approx h_{min}(\tau)$; see figure 2(a). This result is appreciated more clearly in figure 4, which provides the values of $h_m(\tau)$ and $h_{min}(\tau)$ for different values of the Weber and Stokes numbers explored in this study. Indeed, figure 4 reveals that $h_{min}(\tau) = h_m(\tau)$ for the instants of time (highlighted in blue in figure 4) $\tau \leq \tau^*$, and also that $h_m(\tau) > h_{min}(\tau)$ for $\tau > \tau^*$. Due to the fact that the values of the maximum gas pressure, the maximum pressure gradient and also the minimum of $h_m(\tau)$ are attained at $\tau = \tau^*$, the instants of time $\tau < \tau^*$ will be termed, in what follows, as pre-impact stage, whereas those corresponding to $\tau > \tau^*$ will be referred here as post-impact stage; see also the time-evolving dimple shapes included as an inset of figure 2(a). Hence here we will consider that the ‘impact’ takes place when the maximum pressure is attained at $\tau = \tau^*$, so, using the result in (2.6a,b)–(2.7), this event is localized at the radial position $r = R\sqrt{3\tau^* St^{-2/3}} \approx 6R St^{-1/3}$; therefore the minimum thickness of the gas film is attained at the dimensionless instant $\tau = \tau^* \approx 12$ and at the dimensionless radial position $r/R \approx 6 St^{-1/3}$.

The division of the impact process into two well-defined stages is crucial to understanding the differences between the present analysis and the predictions in Mandre & Brenner (2012) and Chantelot & Lohse (2021, 2023), who describe the instants previous to the ‘impact’, namely, the pre-impact stage taking place for $\tau < \tau^*$. In contrast, the predictions in Gordillo & Riboux (2022) were deduced with the purpose of describing both the impact and the post-impact stages, and therefore should be applicable to quantify the different events taking place for $\tau \geq \tau^*$.

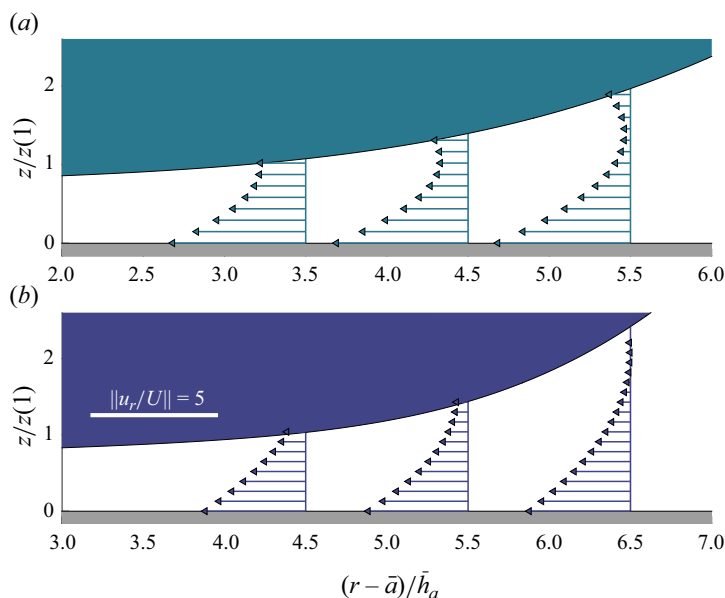


Figure 5. Radial component of the dimensionless gas velocity field, u_r/U , represented in the frame of reference moving with the wetting velocity V_m given in (3.3) for three different values of $(r - \bar{a})/\bar{h}_a$ and two different instants of time: (a) $\tau = 20$ and (b) $\tau = 40$. Here, $\bar{a} \approx R\sqrt{3s}$ indicates the radial position where the maximum gas pressure is attained (see figure 3) and $\bar{h}_a = 2/(9\pi)\bar{a}^3 \approx h_{a,m}$, with $h_{a,m}$ given in (3.4). Here, $We = 12$, $St = 2.60 \times 10^4$, whereas $z(1)$ indicates the vertical coordinate of the interface at the minimum value of $(r - \bar{a})/\bar{h}_a$ represented in the figure.

The next section is devoted to checking which of the predictions for the minimum film thickness – either the ones deduced in Mandre & Brenner (2012) or those in Gordillo & Riboux (2022) – are in better agreement with the numerical results.

3. Modelling the impact of drops over isothermal substrates

3.1. Review of previous results

The predictions in Mandre & Brenner (2012), later extended by Chantelot & Lohse (2021, 2023) to the case of superheated substrates, are based on the following idea: the minimum gas film thickness is attained when a self-similar solution describing the pre-impact stage at the region where the distance to the wall is minimum, fails to predict the flow for $\tau \geq \tau^*$ because the capillary and convective terms in the momentum equation, initially neglected, become of the order of the dominant terms in the approximate solution. Hence, as far as we understand, the results in Mandre *et al.* (2009), Mandre & Brenner (2012) and Chantelot & Lohse (2021, 2023) have been deduced using an argument that neither describes nor identifies the physical mechanism that prevents the contact between the liquid and the wall.

In contrast, the physical model in Gordillo & Riboux (2022) describes the lubricated impact of a drop over a wall for instants of time $\tau \geq \tau^*$. The physical idea behind the predictions in Gordillo & Riboux (2022) relies on the well-known lubrication mechanism depicted in figure 5, where the gas velocity field calculated numerically along the region where the gas pressure is maximum, is represented in a frame of reference radially moving with the wetting velocity at which the local maximum pressure propagates radially outwards,

namely (see figures 2 and 3)

$$V_m(s) = \frac{da}{dt} = \frac{U}{2} \sqrt{\frac{3}{s}}, \quad (3.1)$$

where the subscript m is used to denote the values of quantities particularized at $r = a(s)$; see (2.7). Figure 5 shows that in the moving frame of reference, the gas velocity field can be expressed as the superposition of the Poiseuille (parabolic) velocity profile induced by the favourable pressure gradient pointing radially outwards, towards the atmosphere (see figure 2*b*), plus the Couette (linear) velocity profile caused by the relative motion between the point of maximum pressure and the wall, which is directed towards the axis of symmetry. Notice that the point of maximum pressure is attained at the radial position where the liquid interfacial velocity in the laboratory frame of reference equals the velocity of the moving frame of reference; see e.g. Wagner (1932) and Gordillo & Riboux (2022).

Hence, for the case of isothermal substrates, the distance between the drop and the wall at $r = a(s)$ during the instants close to the one for which the minimum film thickness is attained, can be quantified through the equation (Gordillo & Riboux 2022)

$$-\frac{h_m^3}{12\mu_a} \frac{\partial p}{\partial r} - \frac{V_m h_m}{2} \approx 0. \quad (3.2)$$

Non-continuum effects, which could have been retained in (3.2) by considering values for the slip lengths at the interface and at the wall different from zero (see e.g. Duchemin & Josserand (2012) and Riboux & Gordillo (2014)), will be considered in §4 using the approach detailed in Li (2016) in his numerical study of the head-on collision of drops. This approximation consists in modifying the value of the actual viscosity by using the equation for the effective viscosity deduced in Zhang & Law (2011), which depends explicitly on the Knudsen number defined in terms of the gas film thickness. While gas kinetic effects need to be retained in order to compare our predictions with experiments, van der Waals effects can be neglected safely in the modelling because these forces become relevant only when $h_m \lesssim 20$ nm (Sprittles 2024), namely, for values of the gas film thicknesses that are well below those measured experimentally by de Ruiter *et al.* (2012) for the case of isothermal impacts, and by Chantelot & Lohse (2021, 2023) for the case of drops impacting the wall in the dynamic Leidenfrost regime.

Notice that (3.2) expresses that the value of the Poiseuille flow rate per unit length induced by the large pressure gradient generated around $r = a(s)$ (see figure 3) needs to be balanced by the Couette flow because, otherwise, the gas beneath the region where the pressure is maximum would flow radially outwards, emptying this volume, and consequently the liquid would make contact with the wall.

In order to deduce an equation for h_m , the next step that we followed in Gordillo & Riboux (2022) was to make use of the fact that the vertical interfacial velocities during $\tau \geq \tau^*$ are much smaller than the impact velocity, i.e. $(1/U)\partial h/\partial t \ll 1$, and also that the gas film is slender, $\partial h/\partial r \ll 1$. In this way, since the Reynolds number verifies $Re = St \mu_a/\mu \gg 1$, and hence the production of vorticity at the gas–liquid interface is confined within small boundary layers, the liquid velocity and pressure fields can be approximated by the irrotational values calculated using Wagner’s theoretical framework Wagner (1932). At this point, notice that the condition $(1/U)\partial h/\partial t \ll 1$ also implies that $\ell dh_m/dt \ll V_m h_m$ – with ℓ indicating the characteristic length along which h_m varies, of the order of $\sim h_m$ – due to the fact that $\ell > h_m$ and also because $V_m \propto U St^{1/3} \gg U$, this being the reason why the term $\ell dh_m/dt$ has been neglected in the mass balance (3.2).

Therefore, Wagner’s potential flow theory (Wagner 1932) predicts that the component of the liquid velocity parallel to the wall at $r \approx a(\tau)$ (see also Appendix C, where we discuss the role played by the gas shear stresses) can be expressed as

$$V_m(\tau) = U \frac{\sqrt{3}}{2} \tau^{-1/2} St^{1/3}, \tag{3.3}$$

where use of (2.6a,b) and (3.1) has been made, and Wagner’s theory also predicts that the length along which the liquid interfacial velocity changes of the order of V_m is

$$h_{a,m}(\tau) = R \frac{\sqrt{12\tau^3}}{3\pi} St^{-1}; \tag{3.4}$$

see Gordillo & Riboux (2022) for details. Moreover, Wagner’s theoretical framework (Wagner 1932) also reveals that the tangential liquid velocity changes from V_m to $2V_m$ in a region of width $h_{a,m}$ located around $r = a(s)$, and therefore in the moving frame of reference where (3.2) applies, there exists a stagnation point of the flow. Then, by virtue of the Euler–Bernoulli equation and of fact that the local flow is quasi-steady in the moving frame of reference, the relative pressure with respect to that of the surrounding atmosphere at the stagnation point reads

$$\Delta p_m(\tau) = \frac{1}{2} \rho V_m^2 = \frac{3}{8\tau} \rho U^2 St^{2/3}. \tag{3.5}$$

Consequently, the expression for $h_m(\tau)$ follows from (3.2) once we approximate the pressure gradient as (see figures 2 and 3)

$$-\frac{\partial p}{\partial r} \sim \frac{\Delta p_m(\tau)}{\ell(\tau)} = \frac{1}{2} \rho \frac{V_m^2}{\ell(\tau)}, \tag{3.6}$$

with $V_m(\tau)$ and $\Delta p_m(\tau)$ given in (3.3) and (3.5), respectively. In (3.6), $\ell(\tau)$ refers to the characteristic length where the gas pressure varies of the order of $\sim O(\Delta p_m)$, and hence (Gordillo & Riboux 2022)

$$\left. \begin{aligned} \text{if } \ell_c < h_{a,m}, \text{ then } \ell &= h_{a,m}; \\ \text{if } \ell_c > h_{a,m}, \text{ then } \ell &= \ell_c. \end{aligned} \right\} \tag{3.7}$$

Indeed, in (3.7), ℓ_c indicates the characteristic capillary length where capillary forces balance the pressure in (3.5), namely (Gordillo & Riboux 2022)

$$\frac{\sigma h_m}{\ell_c^2} \propto \Delta p_m \Rightarrow \ell_c(\tau) \propto \sqrt{\frac{\sigma h_m}{\Delta p_m}} = R We^{-1/2} \sqrt{\frac{h_m}{R}} \left(\frac{V_m}{U}\right)^{-1}. \tag{3.8}$$

The substitution of (3.3)–(3.6) into (3.2) yields the following equation for h_m/R :

$$y \left(-1 + \frac{1}{6} y\right) = 0, \tag{3.9}$$

with

$$y = \frac{St}{2(\ell/R)} \frac{V_m}{U} \left(\frac{h_m}{R}\right)^2, \tag{3.10}$$

and therefore,

$$y = 6 \quad \text{and} \quad \frac{h_m}{R} = \left(12 St^{-1} \left(\frac{V_m}{U} \right)^{-1} \frac{\ell}{R} \right)^{1/2}. \quad (3.11)$$

Then, by virtue of (3.7), if $\ell_c > h_{a,m}$, then $\ell/R = \ell_c/R$, hence (3.8) and (3.11) yield the following expression for h_m/R under the so-called capillary regime:

$$\frac{h_{m,c}}{R} \propto y^{2/3} \tau^{2/3} We^{-1/3} St^{-10/9}. \quad (3.12)$$

From this, using (3.8), we deduce the following expression for ℓ_c/R :

$$\frac{\ell_c}{R} \propto y^{1/3} \tau^{5/6} We^{-2/3} St^{-8/9}. \quad (3.13)$$

In contrast, if $h_{a,m} > \ell_c$, then $\ell/R = h_{a,m}/R$ (see (3.4) and (3.7)), and the expression for h_m/R in the so-called inertial regime follows from the definition of y in (3.10):

$$\frac{h_{m,i}}{R} \propto y^{1/2} \tau St^{-7/6}. \quad (3.14)$$

Then the parameter controlling whether the minimum film thickness is given by either the capillary equation (3.12) or the inertial equation (3.14) is the ratio (see (3.4), (3.7) and (3.13))

$$\frac{h_{a,m}}{\ell_c} = We^{2/3} y^{-1/3} St^{-1/9} \tau^{2/3} = \bar{\xi}^{2/3}, \quad (3.15)$$

where

$$\bar{\xi} = \tau \xi, \quad \text{with} \quad \xi = We St^{-1/6} y^{-1/2} \quad (3.16)$$

and, consequently, all the results deduced above can be summarized, making use of (3.6), as follows.

$$\left. \begin{aligned} \text{If } \xi \lesssim \xi^*, \text{ then } \frac{h_{m,c}}{R} &= Ay^{2/3} \tau^{2/3} We^{-1/3} St^{-10/9} \text{ and } -\frac{\partial p}{\partial r} \propto \frac{\rho U^2}{R} \tau^{-11/6} St^{14/9} We^{2/3} y^{-1/3}. \\ \text{If } \xi \gtrsim \xi^*, \text{ then } \frac{h_{m,i}}{R} &= By^{1/2} \tau St^{-7/6} \text{ and } -\frac{\partial p}{\partial r} \propto \frac{\rho U^2}{R} \tau^{-5/2} St^{5/3}. \end{aligned} \right\} \quad (3.17)$$

Here, A and B are order unity prefactors to be determined in § 3.2, and the corresponding expressions for the pressure gradients have been obtained making use of (3.6)–(3.7). Indeed, the substitution of the equations for V_m/U and ℓ/R given in (3.3) and (3.7) into (3.11) would give $A \approx 6$ and $B \approx 2$, but these are only approximate values, which will be quantified accurately in § 3.2 using the results of the numerical simulations. Let us anticipate here that the analysis in § 3.2 will also reveal that the correct value of ξ^* – namely, of the threshold value of ξ separating the capillary and inertial regimes – is $\xi^* \approx 3.5$, which is substantially larger than the *ad hoc* threshold value $\xi^* = 6^{-1/2}$ that we used in Gordillo & Riboux (2022).

Notice that the result corresponding to the capillary-dominated regime in (3.17) was already obtained by Duchemin & Josserand (2011), but using a type of approach different to the one followed here. Indeed, among other things, the lubrication equations in

Duchemin & Josserand (2011) do not satisfy the continuity of the tangential velocities at the interface, therefore the term representing the Couette contribution to the flow rate is missing in their approximate description, this being a key ingredient of the physical model presented in Gordillo & Riboux (2022), based on the classical lubrication mechanism illustrated in figure 5, which we improve here by retaining gas kinetic effects, as will be detailed below. In addition, here we extend the analysis corresponding to the capillary and inertial regimes in Gordillo & Riboux (2022) with the purpose of describing the so-called lift-off mechanism described by Kolinski *et al.* (2014*b*); hence here we include the dependence with time in the equations for the minimum film thickness. Moreover, the values of the prefactors A and B in (3.17) corresponding to the case of low viscous liquids will also be provided here; indeed, in view of the results in Mishra *et al.* (2022), these two values could also depend on the viscosity ratio.

3.2. Comparison between predictions and the numerical results

The two expressions for the minimum film thickness in (3.17) depend on the value of the parameter ξ defined in (3.15)–(3.16), which expresses a measure of the relative importance between the capillary and the dynamic pressure given in (3.5). In this way, values of the parameter ξ such that $\xi > \xi^*$ indicate that capillary effects are subdominant and the impact can be considered as inertial, whereas in the opposite limit, capillary effects can no longer be neglected, and the drop impacts the wall in the so-called capillary regime. Likewise, Mandre & Brenner (2012) deduced the following equations, analogous to those given in (3.17) depending on whether or not capillary effects can be neglected.

$$\left. \begin{aligned} \text{Capillary regime: } \frac{h_{mc,MB}}{R} &\propto We^{-2/3} St^{-8/9}. \\ \text{Inertial regime: } \frac{h_{mi,MB}}{R} &\propto St^{-4/3}. \end{aligned} \right\} \quad (3.18)$$

In order to decipher which of the two different predictions is in closer agreement with the numerical results – namely, either that deduced by Mandre & Brenner (2012) (and later used by de Ruiter *et al.* 2012; Chantelot & Lohse 2023) or the more recent ones in Gordillo & Riboux (2022) – we compare in figure 6 the ratios between the numerical values of the minimum gas film thickness calculated at $\tau^* = 12$, $h_{min}(\tau = 12)$, and the predictions given in (3.17) and (3.18). The results depicted in figure 6, where the proportionality constants in (3.17) and (3.18) have been selected in order to maximize the agreement with the numerical values, reveal that our predictions in (3.17) reproduce the numerical results better using, in addition, prefactors of order unity, namely $A = 3.5$ and $B = 1$, which are similar to the ones obtained by substituting the values of V_m/U and ℓ/R given in (3.3) and (3.7) into (3.11), i.e. $A \approx 6$ and $B \approx 2$.

As pointed out already, figure 7 shows that the values of h_{min} and h_m are very similar to each other up to $\tau = \tau^*$. Beyond that instant of time, the values of h_{min} keep on decreasing but very smoothly, so that the curve corresponding to h_m lies above the one for h_{min} for $\tau > \tau^*$. Figure 7 also compares the results of numerical simulations with the time-dependent predictions given in (3.17), once the origin of times is fixed appropriately. Indeed, notice that the virtual origin of times is set in figure 7 at a dimensionless instant $\tau' = -3$, a value that is consistent with the time taken to entrap the central bubble. This result, which could be interpreted as if the impact began before the drop reaches the wall, shares similarities with previous findings on the subject; see e.g. Peters *et al.* (2013), where both numerical

The skating of drops impacting over gas or vapour layers

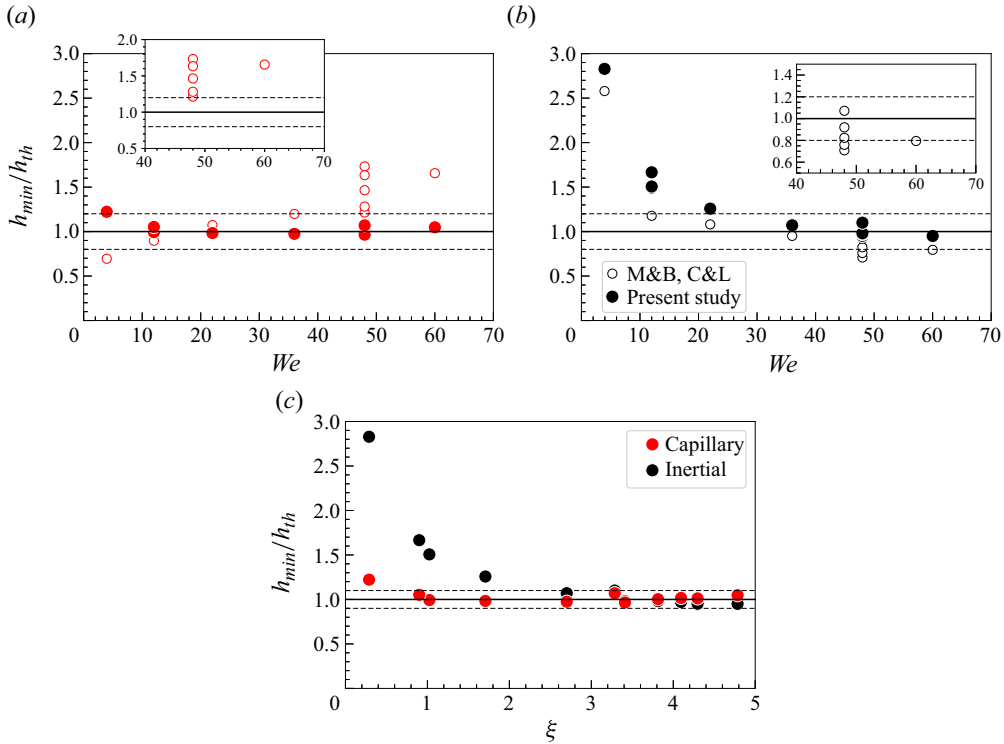


Figure 6. Comparison between the numerical values of the minimum gas layer thickness calculated as $h_{min}(\tau^* = 12)$ and the predicted values h_{th} , given either in (3.18) (Mandre & Brenner 2012; Chantelot & Lohse 2023) or in (3.17) (Gordillo & Riboux 2022) for the case of isothermal substrates, $y = 6$. The predicted values in (a,b) correspond, respectively, to the capillary and inertial regimes in (3.17) and (3.18). The values predicted by Mandre & Brenner (2012) (M&B) and Chantelot & Lohse (2023) (C&L) are represented using open symbols (\circ): in (a), $h_{th} = 17.0R We^{-2/3} St^{-8/9}$, whereas in (b), $h_{th} = 180.0R St^{-4/3}$. The values corresponding to the predictions in Gordillo & Riboux (2022) are represented using full symbols (\bullet): in (a), $h_{th} = 3.5R\tau^{*2/3}y^{2/3} St^{-10/9} We^{-1/3}$, whereas in (b), $h_{th} = 1.0R\tau^* St^{-7/6} y^{1/2}$. Dashed lines indicate variations $h_m/h_{th} = 1.0 \pm 0.2$. (c) Comparison between the numerical results and the theoretical predictions in (3.17) as a function of $\xi = We St^{-1/6} y^{-1/2}$, with h_{th} calculated as $h_{th} = 3.5R\tau^{*2/3}y^{2/3} St^{-10/9} We^{-1/3}$ for the case of the capillary regime, or as $h_{th} = 1.0R\tau^* St^{-7/6} y^{1/2}$ for the case of the inertial regime. In (c), dashed lines indicate variations $h_m/h_{th} = 1.0 \pm 0.1$.

and experimental results reveal that the gas cushioning effects can be quantified using a virtual origin of times, or the numerical results in Ross & Hicks (2019), which show that a two-dimensional impacting solid deforms the interface before contacting the liquid.

Interestingly, the results in figure 7 are the manifestation of the so-called ‘lift-off instability’, described empirically by Kolinski *et al.* (2014b) and analysed very recently using two-dimensional numerical simulations by Mishra *et al.* (2022). Indeed, figure 7 shows that, consistently with our predictions, the growth in time of the minimum film thickness can be quantified using either the capillary or the inertial limits of (3.17), depending on whether the value of the parameter ξ is larger or smaller than $\xi^* \approx 3.5$. The fair agreement between predictions and numerical results in figure 7 indicates that the lift-off instability corresponding to low values of the liquid to gas viscosity ratio can be

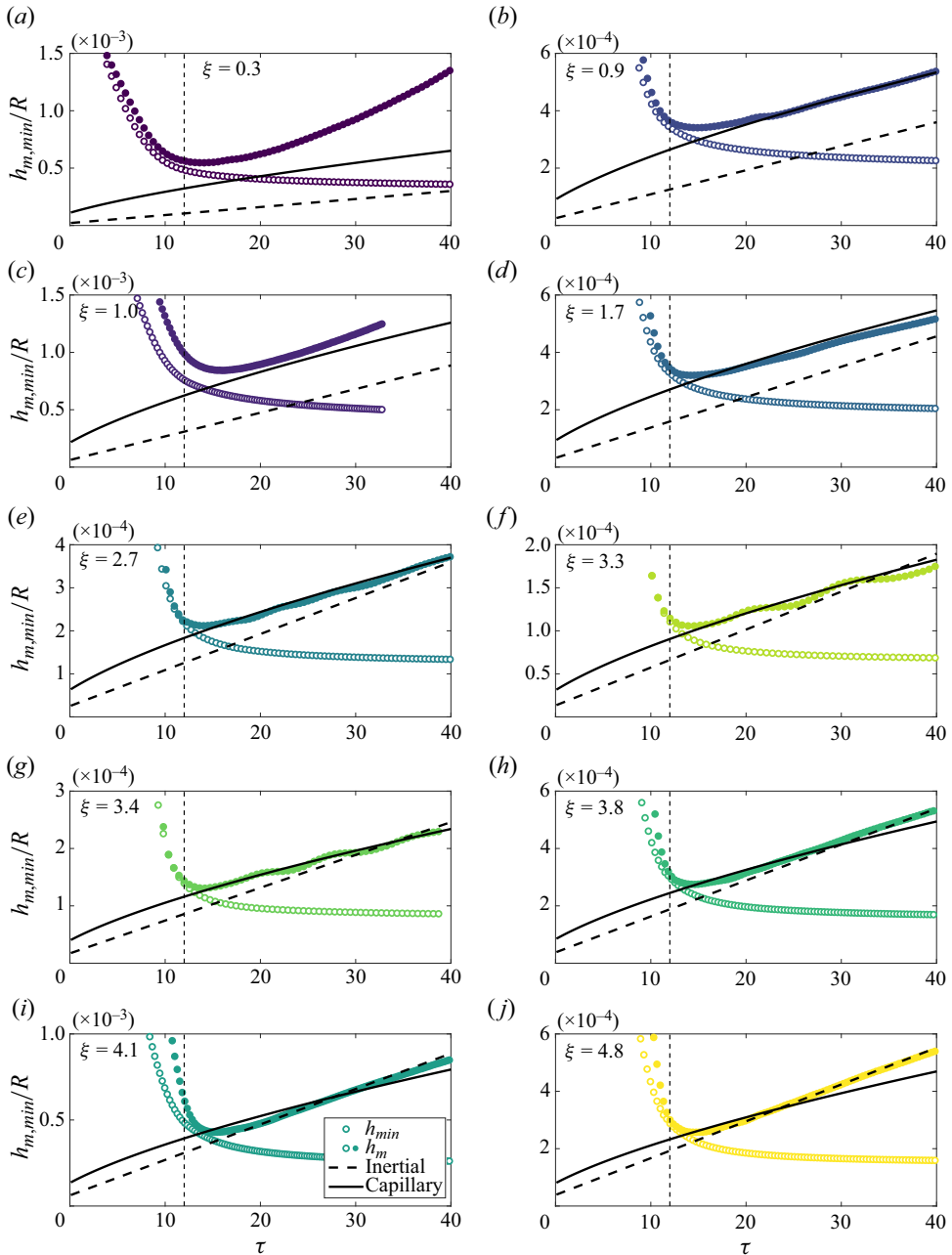


Figure 7. Comparison between the numerical values of $h_{min}(\tau)$ (empty symbols) and $h_m = h(r/R = \sqrt{3}s, \tau)$ (full symbols), with the values predicted in (3.17) for the case of isothermal substrates, $y = 6$, using the following values for the prefactors: $h_m/R = 2.42 y^{2/3} (\tau - \tau')^{2/3} We^{-1/3} St^{-10/9}$ (solid lines) or $h_m/R = 0.48 y^{1/2} (\tau - \tau') St^{-7/6}$ (dashed lines), with $\tau' = -3$. In each of the plots, the thin vertical dashed line shows the value $\tau = 12$. Values are: (a) $We = 4$, $St = 3.0 \times 10^4$; (b) $We = 12$, $St = 2.6 \times 10^4$; (c) $We = 12$, $St = 1.2 \times 10^4$; (d) $We = 22$, $St = 2.1 \times 10^4$; (e) $We = 36$, $St = 2.6 \times 10^4$; (f) $We = 48$, $St = 4.5 \times 10^4$; (g) $We = 48$, $St = 3.6 \times 10^4$; (h) $We = 48$, $St = 1.8 \times 10^4$; (i) $We = 48$, $St = 1.2 \times 10^4$; (j) $We = 60$, $St = 1.8 \times 10^4$.

quantified using the equations below.

$$\left. \begin{aligned} \text{If } \xi \lesssim 3.5, \text{ then } \frac{h_{m,c}}{R} &= 2.42y^{2/3}(\tau + 3)^{2/3} We^{-1/3} St^{-10/9}. \\ \text{If } \xi \gtrsim 3.5, \text{ then } \frac{h_{m,i}}{R} &= 0.48y^{1/2}(\tau + 3) St^{-7/6}. \end{aligned} \right\} \quad (3.19)$$

Notice that the values of the prefactors in (3.19), $A = 2.42$ and $B = 0.48$, are not the same as those deduced from figure 6, $A = 3.5$ and $B = 1$; the reason for these slight differences lies in the fact that the numerical values in figure 6 correspond to $h_{min}(\tau = 12)$, namely, to an instant of time around which the transition between the pre-impact and post-impact stages depicted in figure 4 takes place, whereas the values predicted in (3.19) correspond to $h_m(\tau > 12)$, namely, within the post-impact stage described by our model; see figure 7. Then the small differences in the values of the proportionality constants are caused by the fact that the results in figure 6 correspond to an instant of time that is slightly smaller than that from which our modelling starts being valid, as it is evidenced by the fact that the actual function $h_m(\tau)$ depicted in figure 7 possesses a minimum at $\tau \approx 12$, whereas our (3.19) predict that h_m increases monotonically with τ . In fact, the results in figure 6 indicate that the expressions for h_m corresponding to the post-impact stage deduced here can be used to describe the minimum film thickness at the instant of time $\tau = 12$, at which the analysis is not strictly valid, by simply introducing slight changes in the values of the constants A and B in (3.19). Let us point out here that we could not include in figure 7 the analogous predictions by Mandre & Brenner (2012) and Chantelot & Lohse (2023) because these authors limited their analysis to the instant when the minimum film thickness is attained, therefore their results do not depend on time.

Appendix B compares the numerical values of the pressure and the pressure gradient with the predictions given in § 3.1, providing further support to our physical description.

4. Comparison between predictions and experiments

4.1. Modelling the vapour production and the inclusion of gas kinetic effects

A previous step before comparing our predictions with the experimental measurements is to add to (3.2) the term representing the flow rate per unit length q_v produced by the evaporation of the liquid. Indeed, as explained in the Introduction, we will consider here not only the case of isothermal impacts already analysed in §§ 2 and 3, but also the case of drops impacting over superheated substrates, i.e. substrates with temperature $T_s > T_b$, with T_b indicating the boiling temperature of the liquid. Then, in order to predict the experimental measurements for the minimum film thickness reported in Chantelot & Lohse (2021, 2023), where $\Delta T = T_s - T_b$ is varied within an ample range of values, we make use here of the result in Sobac *et al.* (2014), which provided the following expression for the flow rate per unit length of vapour produced in a region of length ℓ , where the distance between the liquid and the wall is h_m :

$$q_v \approx \frac{k_v \Delta T}{\rho_v \mathcal{L}} \frac{\ell}{h_m}. \quad (4.1)$$

In (4.1), \mathcal{L} refers to the latent heat of vaporization of the liquid, and the viscosity, density and thermal conductivity of the vapour will be denoted in what follows as μ_v , ρ_v and k_v . Notice that (4.1) expresses the balance between the conductive heat flux from the substrate into the drop and the evaporation rate of the liquid at the interface; indeed, we justified

in Gordillo & Riboux (2022) that the heat flux across the liquid thermal boundary layer can be neglected for the particular case of the experiments reported in Chantelot & Lohse (2021, 2023).

Therefore, the equation analogous to (3.2) for the case of drops impacting over superheated substrates reads

$$-\frac{h_m^3}{12\mu_v} \frac{\partial p}{\partial r} - \frac{V_m h_m}{2} \approx \frac{k_v \Delta T}{\rho_v \mathcal{L}} \frac{\ell}{h_m}, \tag{4.2}$$

where we have made use of (4.1). The substitution of (3.3)–(3.6) into (4.2) yields the following equation for h_m/R :

$$y \left(-1 + \frac{1}{6} \frac{\mu_a}{\mu_v} y \right) = \beta^*, \tag{4.3}$$

with

$$y = \frac{St}{2(\ell/R)} \frac{V_m}{U} \left(\frac{h_m}{R} \right)^2 \quad \text{and} \quad \beta^* = \beta \left(\frac{\rho}{\rho_v} \right) \left(\frac{\mu_v}{\mu_a} \right), \quad \text{where} \quad \beta = \frac{k_v \Delta T}{\mu_v \mathcal{L}}. \tag{4.4}$$

Consequently,

$$\frac{h_m}{R} = \left(2y St^{-1} \left(\frac{V_m}{U} \right)^{-1} \frac{\ell}{R} \right)^{1/2}, \tag{4.5}$$

with

$$y = 3 \left(\frac{\mu_v}{\mu_a} \right) \left[1 + \sqrt{1 + \frac{2\beta^*}{3} \left(\frac{\mu_a}{\mu_v} \right)} \right]. \tag{4.6}$$

The substitution of (4.6) and of either (3.4) or (3.8) into (4.5) provides the same expressions as those given in (3.17), which are then valid to describe the skating of drops over either a gas or a vapour layer, the only difference being that $y = 6$ for the case of isothermal impacts, whereas y is given by (4.4) and (4.6) for the cases of drops impacting a substrate in the dynamic Leidenfrost regime. Hence our physical description differs substantially from that of Chantelot & Lohse (2021, 2023), who deduce different equations depending on whether the substrate is superheated or not, therefore the isothermal case cannot be recovered using their results corresponding to superheated substrates in the limit in which the production of vapour tends to zero.

The recent review on the subject by Sprittles (2024) states clearly that gas kinetic effects cannot be neglected in the description of the head-on collision of drops (Li 2016) or in the impact of drops on a substrate (Riboux & Gordillo 2014; Chubynsky *et al.* 2020) if the value of the Knudsen number, defined as

$$Kn = \frac{\lambda}{h_m}, \tag{4.7}$$

with λ denoting the mean free path of the gas, becomes $Kn \gtrsim 0.1$, which is the case of interest here. Indeed, the typical values of the gas film thickness in the experiments reported by de Ruiter *et al.* (2012) and Chantelot & Lohse (2021, 2023) vary between 10^3

and 10^2 nanometres, whereas the values of the mean free path of air and ethanol at normal conditions are, respectively,

$$\lambda_a \approx 69 \text{ nm} \quad \text{and} \quad \lambda_{eth} \approx 50 \text{ nm}. \quad (4.8a,b)$$

Then, in order to account for gas kinetic effects, we define an effective gas viscosity $\mu^*(Kn)$ (Sprittles 2024) and make use of the expression deduced by Zhang & Law (2011), employed successfully by Li (2016) in his study of the head-on collision of drops:

$$\mu^* = \frac{\mu}{1 + 6.0966 Kn + 0.9650 Kn^2 + 0.6967 Kn^3}, \quad (4.9)$$

where μ refers to the value of the actual gas viscosity. Notice that for the case of drops impacting a non-heated substrate, μ_v in (4.6) refers to the effective air viscosity, namely, $\mu_v = \mu_a^*$ (see (4.9)), whereas the Knudsen number defined in (4.7) is calculated using the value of the mean free path given by

$$\lambda = \lambda_a \frac{P_a}{P_a + \Delta p_m}, \quad (4.10)$$

with λ_a and Δp_m given, respectively, in (4.8a,b) and (3.5). For the case of drops impacting a superheated substrate, $\mu_v = \mu_{eth}^*$ and

$$\lambda = \lambda_{eth} \frac{P_a}{P_a + \Delta p_m} \frac{273 + 0.5(T_b + T_s)}{T_a}, \quad (4.11)$$

with $T_a = 298$ K, and $T_b = 78$ and T_s refer to the values in Celsius of the boiling temperature of ethanol and of the substrate temperature, respectively. For the case of drops impacting a superheated substrate, here we also include gas kinetic effects in the heat transfer from the wall into the liquid, making use of the effective heat conductivity for the vapour given by (Sharipov *et al.* 2007)

$$k_v^* = \frac{k_v}{1 + 3.91 Kn}. \quad (4.12)$$

As pointed out in the Introduction, van der Waals effects are not retained in the analysis because in all the experimental results reported by de Ruiter *et al.* (2012) and Chantelot & Lohse (2021, 2023), the gas film thickness is well above 20 nm, which is the length scale below which these forces become relevant (Sprittles 2024).

4.2. Comparison with experiments

The comparison with the numerical results in § 3 confirms our physical description, and it is now our purpose in this subsection to check whether our results, once gas kinetic effects are taken into consideration, can also be used to predict the experimental data reported by de Ruiter *et al.* (2012) and Chantelot & Lohse (2021, 2023) for drops impacting over either isothermal or superheated substrates.

The equations given in (4.6) and (3.17) can be used to predict the minimum gas film thickness for arbitrary values of T_s . However, the unified description for the skating of a drop over a gas or vapour film provided by (4.6) and (3.17) also requires us to introduce the effect of the vapour produced at the dimple on the instant of time τ^* at which the central bubble is formed, i.e. at the instant when the minimum film thickness is attained at $r \approx R St^{-1/3} \sqrt{3\tau^*}$.

Then, for the case of superheated substrates, the term on the left-hand side of the mass conservation equation (2.2) needs to be modified in order to take into account the evaporation of the liquid. Consequently, in this case, the flow rate that needs to be evacuated radially outwards from the axis of symmetry is $\pi(Rh_d)(U + k_v \Delta T / (\rho_v h_d \mathcal{L}))$. Therefore, expressing $h_d/R = \tau^* St^{-2/3}$ and following the same steps as those detailed in § 3, the mass balance (2.2) provides the following equation for τ^* (Gordillo & Riboux 2022):

$$\tau^{*5/2} = 12.4^{3/2} \left(\tau^* + \beta^* St^{-1/3} \right), \tag{4.13}$$

with β^* defined in (4.4). Notice that (4.13) recovers the value of $\tau^* \approx 12$ corresponding to the case of isothermal substrates, for which $\beta^* = 0$.

Before comparing our predictions with the experimental values provided in de Ruiter *et al.* (2012) and Chantelot & Lohse (2021, 2023), it is first necessary to express the real temperature-dependent material properties of the gas and of the vapour as functions of the substrate temperature. This is done here using the Python routines provided as supplementary material available at <https://doi.org/10.1017/jfm.2024.20>, which implement (3.17), (4.6) and (4.7)–(4.12) and make use of the values $\sigma = 22 \times 10^{-3} \text{ N m}^{-1}$ or $\sigma = 17 \times 10^{-3} \text{ N m}^{-1}$ for the interfacial tension coefficient of ethanol at either room or boiling temperature, with these values taken from www.ddbst.com. Notice that all the material properties are quantified at the mean temperature $(T_b + T_s)/2$ as detailed in Gordillo & Riboux (2022), and this is reflected in the Python routines provided as supplementary material. Let us point out here that we have not considered the effect of Marangoni stresses in our physical model because the liquid located at a distance h_m from the wall is evaporating along a region of length ℓ , therefore the interfacial temperature remains constant and equal to the boiling temperature of the liquid at the region of interest here, namely, where the minimum film thickness is attained.

Figure 8 reveals that the minimum gas film thickness can be predicted using the equations corresponding to the capillary or inertial limits in (3.17) and (4.4)–(4.12) with relative errors $\sim 30\%$. For the case of isothermal substrates, the predicted value for the minimum film height has been calculated in figure 8 retaining gas kinetic effects and using the capillary limit in (3.17) with $A = 3.5$, namely, the value deduced from figure 6 for the case of drops impacting a wall at room temperature in the ideal case $Kn = 0$. Hence for the case of substrates at room temperature, we conclude that the experimental data can be approximated using the equation (see (3.17))

$$\frac{h_m}{R} \approx 3.5 \times \left(6 \frac{\mu_a^*}{\mu_a} \right)^{2/3} 12^{2/3} We^{-1/3} St^{-10/9}, \tag{4.14}$$

with $\mu_a^* = \mu^*$ defined in (4.9).

Figure 8 also compares the experimental measurements in Chantelot & Lohse (2021, 2023) with our predictions. In this case, since the vapour layer prevents contact between the liquid and the wall, a transition between the capillary and inertial regimes in (3.17) is observed when the impact velocity increases. In this case, the equations for the minimum film thickness used in the comparisons of figure 8 are (see (3.17))

$$\frac{h_m}{R} \approx 2.3 y^{2/3} \tau^{*2/3} We^{-1/3} St^{-10/9} \tag{4.15}$$

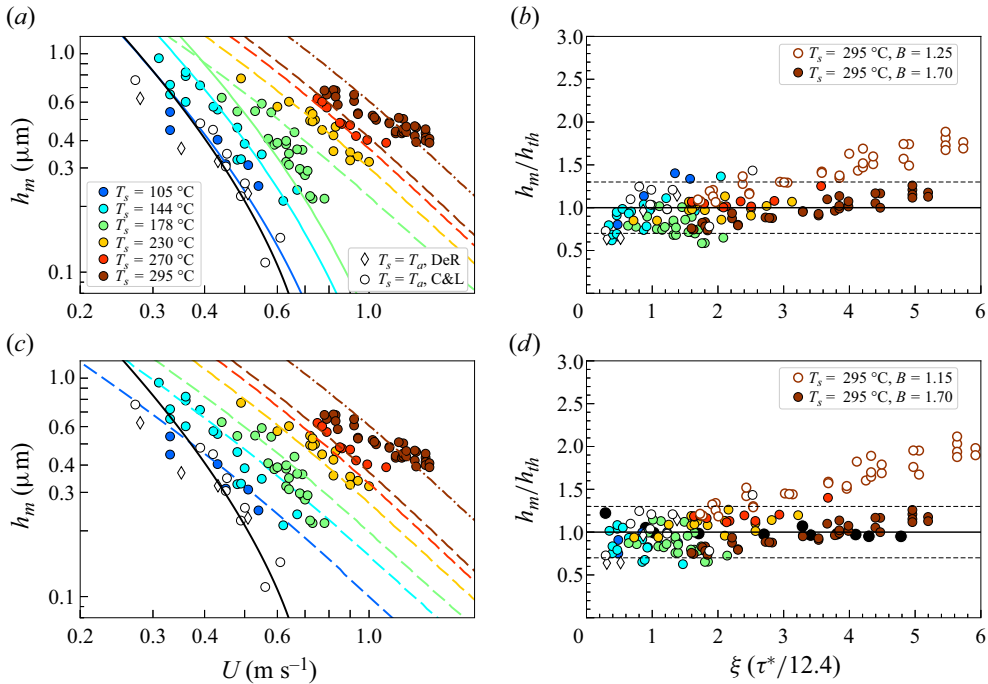


Figure 8. (a) Comparison between the predictions given in (4.14)–(4.16) and the values for the minimum thickness of the air or vapour layers measured by de Ruiter *et al.* (2012) (DeR) and Chantelot & Lohse (2023) (C&L) for different values of the impact velocity U and for different values of the substrate temperature T_s . Here, the values of the effective gas viscosity and the effective gas conductivity have been modified taking into account kinetic effects through (4.7)–(4.12). Solid lines represent the predictions for h_m corresponding to the capillary regime, whereas the predictions for h_m in the inertial regime are represented using dashed lines. (b) Comparison between the predicted and measured values of h_m in (a) as a function of ξ . (c) The experimental data are compared here only with the predictions given by (4.16). In this case, the value of the prefactor is 1.15 instead of 1.25. (d) Comparison between the predicted and measured values of h_m in (c) as a function of ξ . The dashed horizontal lines in (b,d) are placed at 1 ± 0.3 .

and

$$\frac{h_m}{R} \approx 1.25 \tau^* St^{-7/6} y^{1/2} \quad (4.16)$$

for the capillary and inertial regimes, respectively. In (4.15)–(4.16), y is given by (4.6), τ^* has been calculated using (4.13), and gas kinetic effects have been quantified through (4.7)–(4.12). The value of the prefactor in (4.15), corresponding to the capillary limit in (3.17), differs from that in (4.14). This could be due to the differences in the local geometry of the interface for $r \approx a$; indeed, the experiments in figure 3 of Chantelot & Lohse (2021) show that the curvature of the interface near $r \approx a$ for the case of Leidenfrost drops increases with T_s (see also Kolinski *et al.* 2014b), a fact implying that the prefactor affecting ℓ in (4.5) for the case of superheated substrates should be smaller than for the case of isothermal impacts. Notice also that since the local curvature is very much dependent on whether the substrate is superheated or not, it could also be the case that de Ruiter *et al.* (2012) and Chantelot & Lohse (2023) provide the experimental values of $h_{min}(\tau = 12)$ for the case of isothermal substrates, whereas Chantelot & Lohse (2021, 2023) provide $h_m(\tau \approx 12)$ for the case of superheated substrates; in that case, the value of the constant in (4.15) would be very similar to the one in (3.19). Figures 8(c,d)

also show a comparison between the predicted and measured minimum film thicknesses under the approximation followed in Gordillo & Riboux (2022), where we considered that the minimum film thickness could be predicted using the inertial approximation given in (4.16). In this case, figures 8(c,d) show that the experimental measurements by Chantelot & Lohse (2021, 2023) can be predicted reasonably well, with relative errors $\pm 30\%$, using a value 1.15 for the prefactor in (4.16), which is very similar to that deduced from figure 6. Notice also that figure 8 also includes the predicted minimum film thickness corresponding to the largest temperature, $T_s = 295^\circ\text{C}$, when the value of the prefactor in (4.16) is varied from 1.25 to 1.7. A possible reason why an increase in the value of the prefactor improves the comparison with the experimental data for the case of the highest substrate temperature could be the fact that the slender approximation under which (3.17) are deduced breaks for sufficiently large values of T_s . Indeed, the parameter expressing the ratio between the minimum film thickness and the length along which the pressure gradients in the liquid take place, namely,

$$\frac{h_m}{h_{a,m}} \approx y^{1/2} St^{-1/6}, \tag{4.17}$$

where we have made use of (3.4) and (4.16), could become larger than unity for substrate temperatures T_s exceeding the threshold value given by the condition (see (4.17))

$$y^2 \gtrsim St^{2/3} \Rightarrow \frac{k_v(T_s - T_b)}{\mu_v \mathcal{L}} \left(\frac{\rho}{\rho_v} \right) \gtrsim St^{2/3}, \tag{4.18}$$

where use of (4.6) has been made. The results depicted in figure 9 reveal that, indeed, the spatial region where the maximum pressure gradient is attained is clearly not slender for the larger value of T_s because the film thickness is larger than the length along which the liquid pressure gradient takes place. In these cases, since $h_m \approx h_{a,m}$, the capillary pressure is $\sim \sigma h_m/h_{a,m}^2 \sim \sigma/h_{a,m}$, with this value being similar to the liquid overpressure Δp_m given in (3.5) because

$$\frac{\Delta p_m}{\sigma/h_{a,m}} \sim We St^{-1/3}, \tag{4.19}$$

which happens to be of order unity for the experiments corresponding to the largest temperatures reported by Chantelot & Lohse (2023). Then the loss of slenderness for the largest value of T_s implies larger capillary pressures because h_m is not much smaller than $h_{a,m}$, a fact also implying that the values of the gas pressure gradient are smaller than those corresponding to the slender limit in which (3.17) have been deduced. A reduction in the pressure gradient implies larger values of h_m (see (4.2)), and this fact could be behind the result depicted in figure 8 for the case $T_s = 295^\circ\text{C}$. Let us also point out that the discrepancies between the predictions and experimental measurements for the case $T_s = 295^\circ\text{C}$ could also be originated as a consequence of limitations in the temporal resolution of the experiments carried out by Chantelot & Lohse (2023) for the highest impact velocities.

5. Conclusions

In this contribution, we have presented numerical simulations validating the predictions in Gordillo & Riboux (2022), where we described the lubrication mechanism by which a drop falling over a substrate skates over a gas or vapour layer. With the purpose of explaining and quantifying the lift-off mechanism reported empirically by Kolinski *et al.* (2014b) and

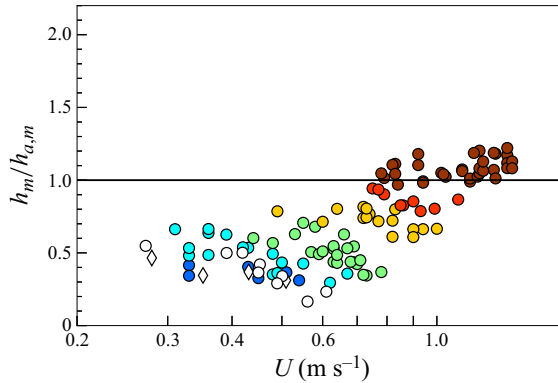


Figure 9. Ratio between the measured minimum film thickness and the length $h_{a,m}$ given in (3.4) along which pressure gradients take place. The meanings of the symbols are the same as in figure 8.

investigated numerically by Mishra *et al.* (2022), we have extended our previous results and have provided equations, including the values of the prefactors, that reproduce closely the time evolution of the minimum film thickness calculated numerically. Moreover, with the purpose of comparing our results with the measured values of the gas or vapour film thicknesses, we have included gas kinetic effects in the algebraic equations for the minimum thickness of the gas layer, finding that our predictions, up to prefactors, are in good agreement with the results reported by de Ruiter *et al.* (2012) and Chantelot & Lohse (2021, 2023).

Supplementary material. Supplementary material is available at <https://doi.org/10.1017/jfm.2024.20>.

Acknowledgements. J.M.G. thanks P. Chantelot and D. Lohse for fruitful discussions.

Funding. This work has been supported by the grant PID2020-115655GB-C21, financed by the Spanish MCIN/AEI/10.13039/501100011033, and all the simulations were run on the High Performance Computing cluster provided by the Centro Informático Científico de Andalucía (CICA).

Declaration of interests. The authors report no conflict of interest.

Author ORCIDs.

P. García-Geijo <https://orcid.org/0000-0001-8608-4804>;

G. Riboux <https://orcid.org/0000-0003-2395-1653>;

J.M. Gordillo <https://orcid.org/0000-0003-1431-3780>.

Author contributions. P.G.-G. carried out the numerical simulations and analysed the data, G.R. analysed the data and partly wrote the paper, and J.M.G. designed the research and the theory, and wrote the paper. All authors reviewed the results and approved the final version of the manuscript.

Appendix A. Numerical simulations

The numerical results in § 2, which have been calculated using the free software Basilisk (Popinet 2015), extending the ideas in the codes by Sanjay (2022) and Zhang *et al.* (2022), simulate the axisymmetric impact of a drop of radius R initially centred at $z = 1.006R$, falling with a uniform velocity U over an impermeable horizontal substrate. The numerical results have been obtained by imposing symmetry conditions at the axis, the impenetrability and no-slip boundary conditions at the wall limiting the computational domain depicted in figure 1, and outflow boundary conditions at the two remaining

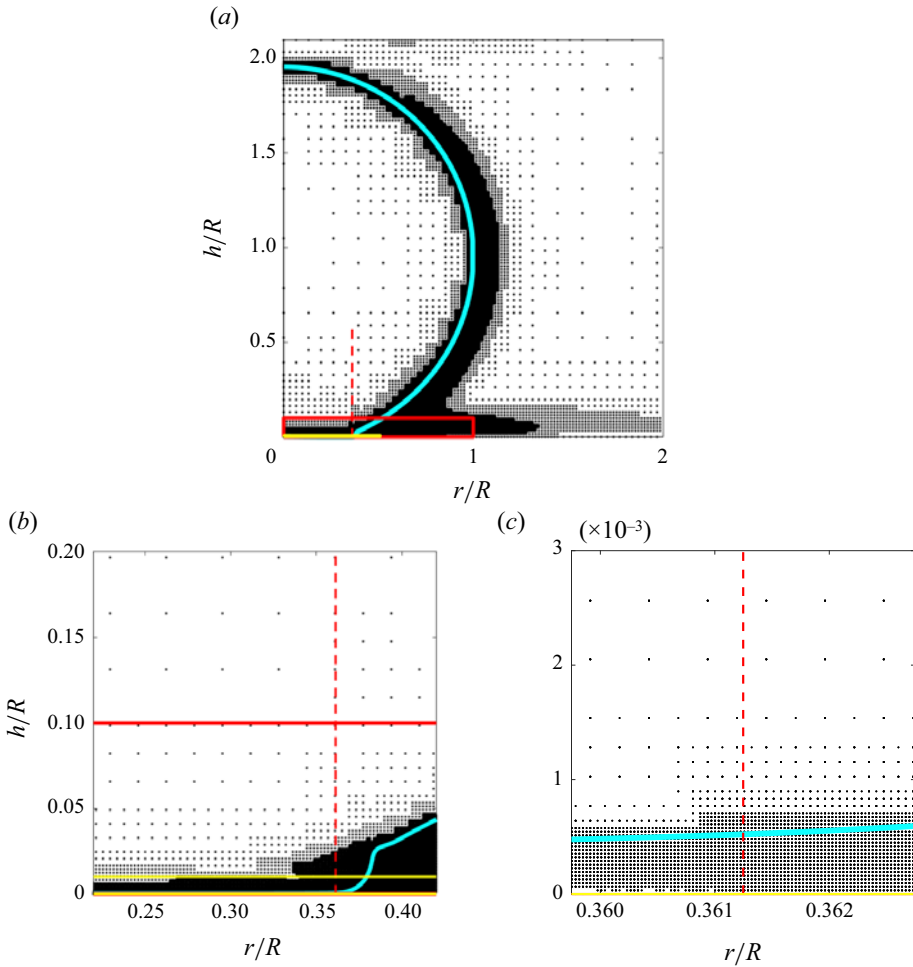


Figure 10. Each black dot represents the vertex of a numerical cell, whereas the interface is plotted using a blue solid line. (a) The numerical domain is divided into regions with different discretization levels: red box, $h/R < 0.1$ and $r/R < 1.0$, with cell sizes $\Delta \geq R/1950$; yellow box, $h/R < 0.01$ and $r/R < \sqrt{3}s + 0.15$, with cell sizes $\Delta \geq R/31208$. For the rest of the numerical domain, $\Delta \geq R/975$. (b) A closer view of the region around the advancing front. (c) Detailed view of the spatial region around the wetting radius $r = \sqrt{3}s$ (red dashed line). Here, $We = 12$, $St = 2.60 \times 10^4$ and $\tau = 0.0435 \approx 38 St^{-2/3}$.

boundaries, where both the pressure and the gradient of normal velocities are set to zero. We have checked that the numerical results are unaffected by the dimensions of the computational domain.

We have made use of an adaptive Cartesian mesh, which refines the solution both at the interface and at the regions with the largest velocity gradients. The tolerances for the volume fraction field, for the velocity field and for the curvature are set to 10^{-3} , 10^{-2} and 10^{-6} , respectively, and the maximum level of grid refinement is defined in each of the different regions into which the computational domain has been divided; indeed, the grid size is $\Delta \geq R/975$ for $z > 0.1$, but $\Delta \geq R/31208$ near the wall, where the velocity and pressure gradients reach the largest values; see the figure 10 caption for details. Moreover, we have carried out a sensitivity analysis in order to verify that the results reported are independent of the grid size; indeed, figure 11 shows that the values of the pressure, the

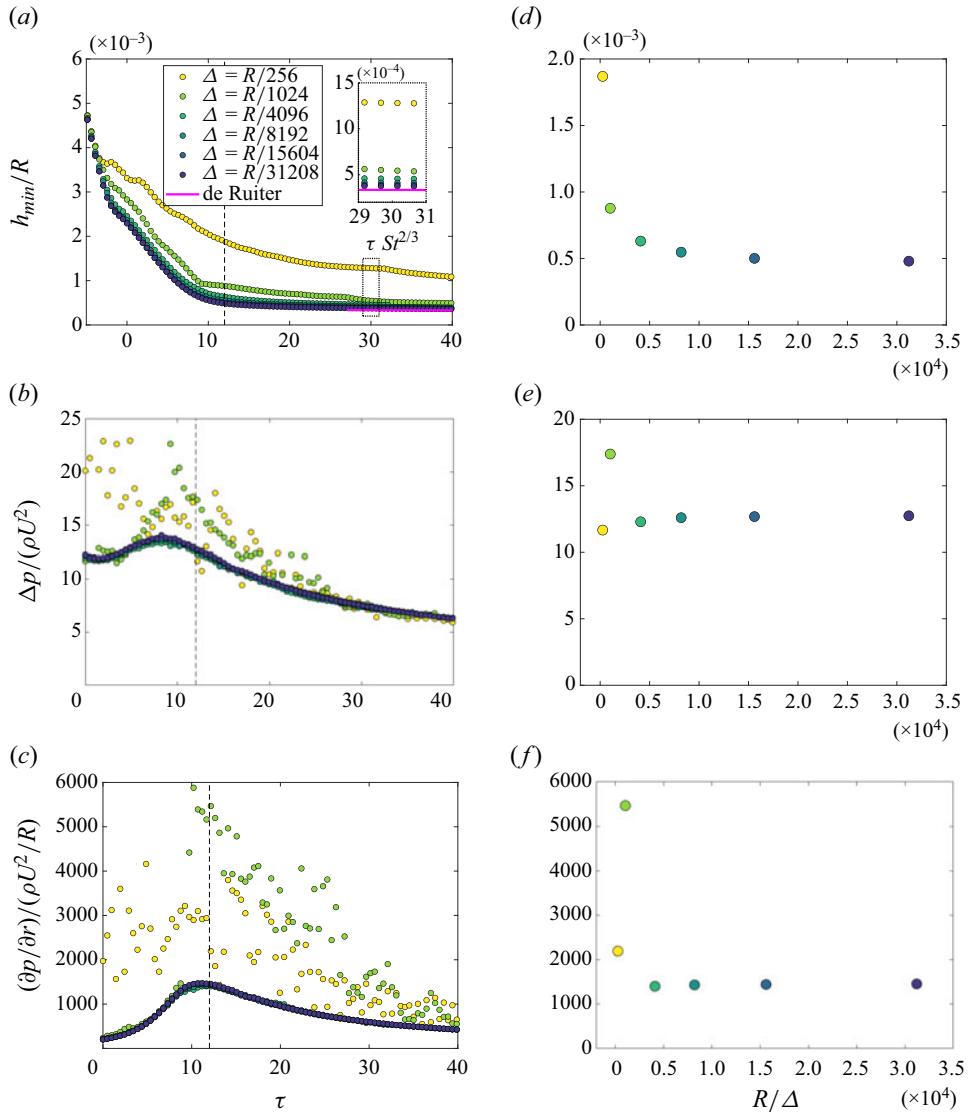


Figure 11. Plots of (a) $h_{min}/R(\tau)$, (b) $\Delta p/(\rho U^2)(\tau)$, and (c) time evolution of $(\partial p/\partial r)R/(\rho U^2)(\tau)$ at the spatio-temporal region where the gas pressure is maximum for different values of the discretization level Δ . The numerical results have been calculated for $We = 4$ and $St = 3 \times 10^4$, which correspond to the values of the dimensionless parameters characterizing a water drop of radius $R = 1.05$ mm impacting a wall with velocity $U = 0.52$ m s⁻¹ reported by de Ruiter *et al.* (2012). The numerical results are compared with the experimental measurements in de Ruiter *et al.* (2012) in the inset of (a). The values of Δ in the legend indicate the minimum grid size. Numerical values at $\tau^* \approx 12$ are given for (d) h_m/R , (e) $\Delta p/(\rho U^2)$ and (f) $(\partial p/\partial r)R/(\rho U^2)$ as functions of R/Δ , with Δ indicating the minimum grid size.

pressure gradient and the minimum gas film thickness become independent of the grid size and converge towards well-defined values. Figure 11 also shows that our numerical results reproduce, with small relative errors, the experimental value of the minimum gas film thickness reported by de Ruiter *et al.* (2012), and table 1 reports the minimum number of cells in the z direction used to compute the gas velocity field within the lubrication layer; see also figures 16 and 17.

We	St	Size
4	3.03×10^4	15
12	1.20×10^4	23
12	2.60×10^4	11
22	2.12×10^4	10
36	2.60×10^4	7
48	1.84×10^4	9
48	3.60×10^4	5
60	1.80×10^4	9

Table 1. Minimum number of numerical cells used to describe the flow in the lubrication layer at the radial position where the thickness of the gas film is minimum. In consequence, the number of cells in the z direction for the rest of the radial positions and instants of times is larger than the values provided in the table.

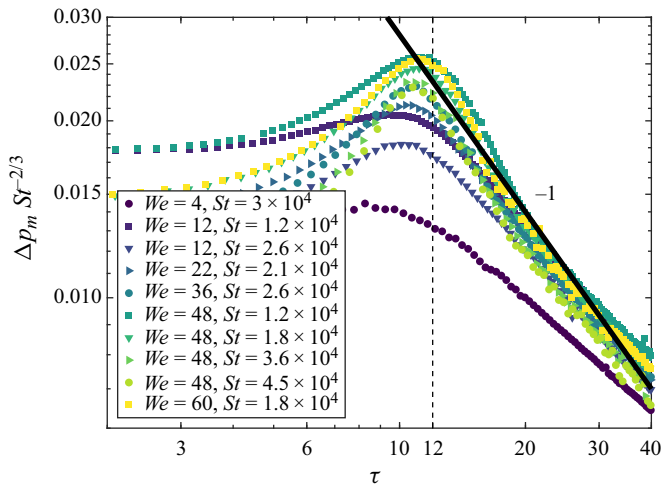


Figure 12. Comparison between the maximum liquid pressure predicted in (3.5) and the maximum gas pressure at the wall for different instants of time and different values of the Weber and Stokes numbers. The dashed line indicates the transition at $\tau^* = 12$ between the pre-impact and post-impact stages.

Appendix B. Comparison between the predicted and calculated values of the gas pressure and the gas pressure gradient

In this contribution, we do not restrict ourselves to validate our physical model with the results shown in figures 6 and 7; indeed, notice here that the equations for the minimum gas film thickness h_m have been deduced through (3.2), which depends on the value of the local pressure gradient at the spatio-temporal region where the pressure is maximum. Hence our predictions for h_m are linked to the correctness of the approximations to the time-dependent values of both the pressure and the pressure gradient given, respectively, in (3.5) and (3.17). This is the reason why figure 12 compares the result in (3.5) with the numerical values of the maximum gas pressure at the wall. Notice that the agreement between predictions and the numerical results improves for increasing values of We due to the fact that the numerical values for the gas pressure depicted in figure 12 are the result of subtracting the capillary pressure from the value of the maximum liquid pressure predicted by (3.5). Moreover, figure 13 shows the time evolution of the pressure gradient at

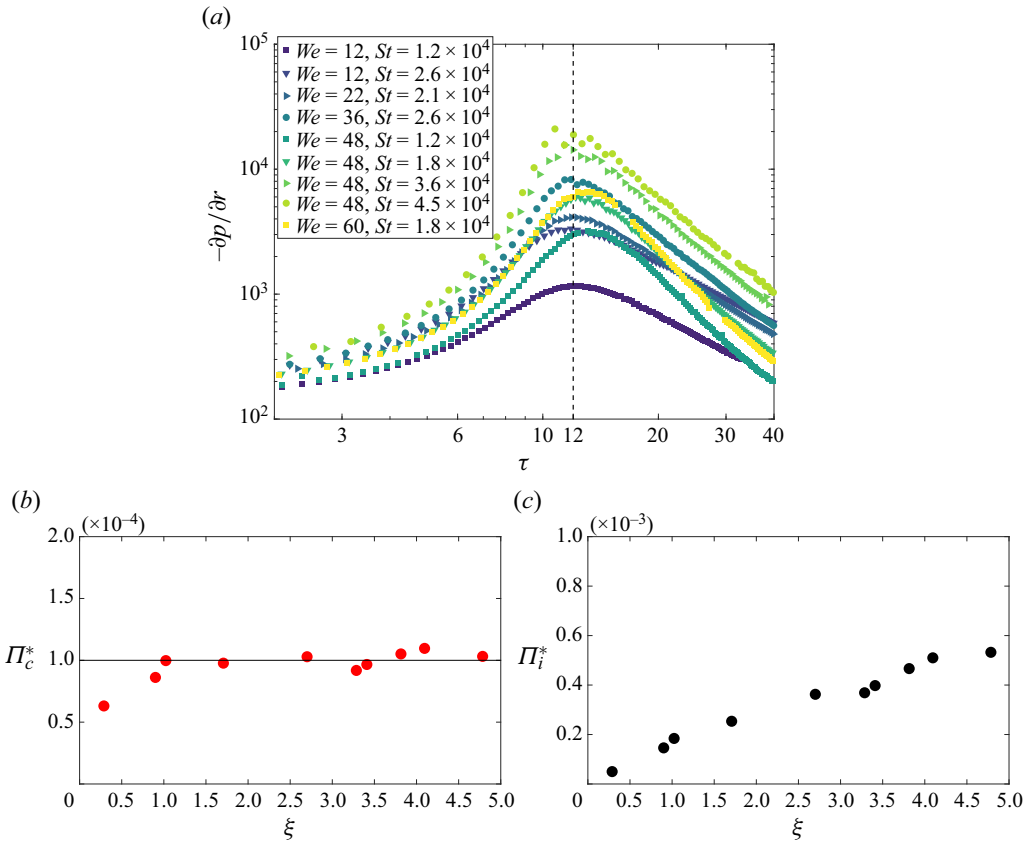


Figure 13. (a) Values of the pressure gradient at the spatio-temporal region where the pressure is maximum for the range of We and St considered in this study. The pressure gradient has been calculated as the slope of the lines tangent to the gas pressure distribution at the wall; see figure 2. (b) The values of the maximum pressure gradients, attained at $\tau = \tau^* \approx 12$, can be predicted well for all values of ξ using the expression for $-\partial p/\partial r$ in (3.17) corresponding to the capillary scaling. (c) The values of the pressure gradient at $\tau = \tau^* \approx 12$ can be predicted well for $\xi \gtrsim 4$ using the expression for $-\partial p/\partial r$ in (3.17) corresponding to the inertial scaling. Here, $\Pi_i^* = \Pi_i(\tau^*) = (-\partial p/\partial r)(\tau^*) St^{-5/3}/(\rho U^2/R)$ and $\Pi_c^* = \Pi_c(\tau^*) = (-\partial p/\partial r)(\tau^*) We^{-2/3} St^{-14/9}/(\rho U^2/R)$.

the region where the pressure is maximum. In both this figure and figure 14, the numerical values of the pressure gradient have been calculated as illustrated in figure 2, namely, as the slope of the lines tangent to the gas pressure distribution at the wall. The results in figures 13(b,c) show that the maximum values of the pressure gradients depicted in figure 13(a) can be predicted using the equations for $-\partial p/\partial r$ given in (3.17) particularized at the instant $\tau = \tau^* \approx 12$. Moreover, figure 14 validates further the predictions given in (3.17) for the time-varying values of the pressure gradient at the spatio-temporal region where the pressure is maximum. Indeed, figure 14(a) shows that the numerical values corresponding to the smaller values of We follow the capillary scaling of $-\partial p/\partial r$ provided in (3.17), whereas figure 14(b) confirms that the values of the calculated pressure gradient for $We \geq 36$ are well captured, specially for the larger values of τ , by the equation corresponding to the inertial limit given in (3.17), as expected from the fact that the transition from the capillary to the inertial regimes is controlled by the value of the parameter $\xi = \tau \xi$; see (3.15)–(3.16).

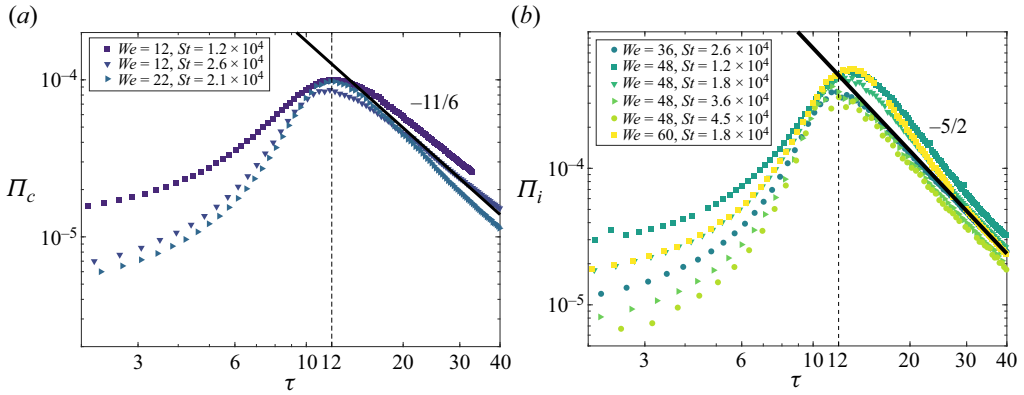


Figure 14. Comparison between the two different expressions for the pressure gradient given in (3.17) and the numerical values calculated as illustrated in figure 2, namely, as the slope of the lines tangent to the gas pressure distribution at the wall. The dashed line indicates the transition at $\tau^* = 12$ between the pre-impact and post-impact stages. In (a), $\Pi_c = -(\partial p/\partial r) We^{-2/3} St^{-14/9}/(\rho U^2/R)$ and the solid line indicates $\propto \tau^{-11/6}$, whereas in (b), $\Pi_i = -(\partial p/\partial r) St^{-5/3}/(\rho U^2/R)$ and the solid line indicates $\propto \tau^{-5/2}$; see (3.17).

Appendix C. Effect of the gas shear stresses on the interfacial liquid velocity

The purpose of this appendix is to analyse the effect of the gas shear stresses on the value of the liquid interfacial velocity. For the case of isothermal substrates, the shear stress balance at the interface yields the following relationship between the jump in tangential velocity across the liquid boundary layer, ΔV_m , and the gas velocity within the thin film $\sim V_m$:

$$\mu \frac{\partial u_r}{\partial z} \sim \mu_a \frac{V_m}{h_m} \Rightarrow \frac{\Delta V_m}{V_m} \sim \frac{\mu_a}{\mu} \frac{\delta}{h_m}, \tag{C1}$$

with

$$\delta \propto \sqrt{\frac{\mu h_d}{\rho U}} \propto R \left(\frac{\mu}{\mu_a} \right)^{1/2} St^{-5/6} \tag{C2}$$

indicating the characteristic thickness of the liquid boundary layer growing during the characteristic time $h_d/U \propto R/U St^{-2/3}$ (Gordillo & Riboux 2022). Then, since $h_m \sim h_{a,m} \sim 15R St^{-1}$ (see (3.4)), (C1) yields

$$\frac{\Delta V_m}{V_m} \sim \left(\frac{\mu_a}{\mu} \right)^{1/2} \frac{St^{1/6}}{15} \ll 1, \tag{C3}$$

a result explaining the mostly uniform velocity profiles within the liquid side of the interface depicted in figure 15, which also shows that the interfacial velocity is $\approx V_m$, with V_m given in (3.1). However, notice also that the numerical results in figure 15 reveal that the radial velocity at the interface reaches the value predicted by Wagner’s theory, $u_r = V_m$, only for sufficiently large values of We and τ . This is a consequence of the fact that the values of We and St in figure 15 correspond to the cases depicted in figures 7(a,d,h), for which capillary pressure cannot be neglected, as it can be inferred from the fact that the values of h_m are very well approximated by the expression corresponding to the capillary regime in (3.19) during the initial stages of the post-impact process, except for the case $We \approx 4$. Then $u_r/V_m < 1$ in figure 15 because when the values of

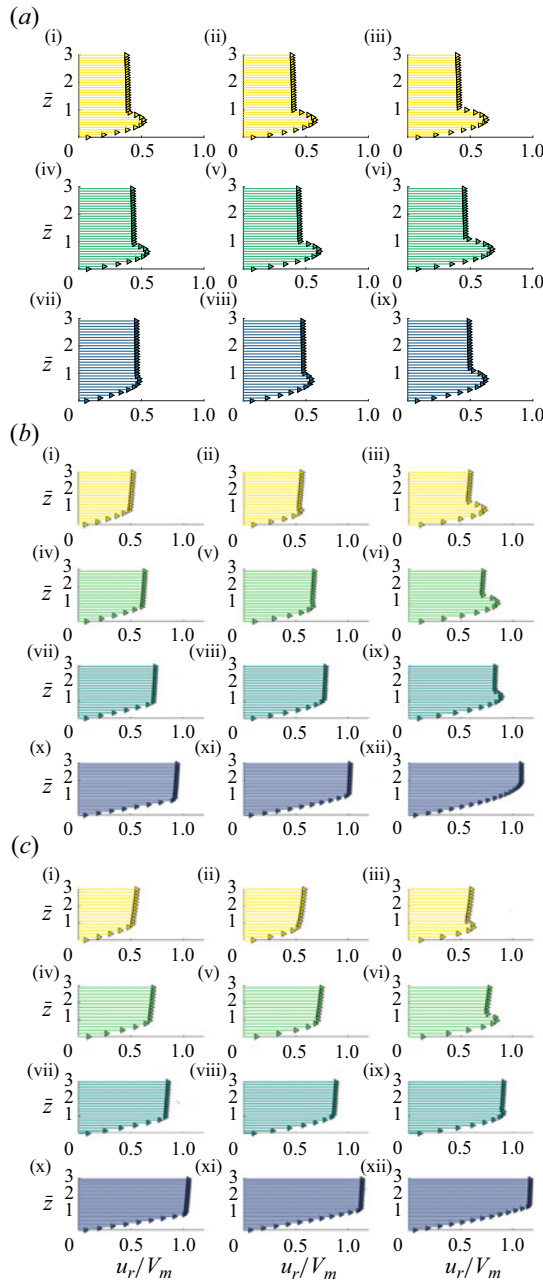


Figure 15. Normalized radial velocity field u_r/V_m as a function of the dimensionless vertical position $\bar{z} = z/z(1)$, with $z(1)$ the vertical coordinate of the interface at different dimensionless times τ , and for different normalized radial positions $(r - \bar{a})/\bar{h}_a$. (a) Here, $We = 3.94$, $St = 3 \times 10^4$ at τ values (a i–a iii) 12, (a iv–a vi) 15 and (a vii–a ix) 20, for the following radial positions $(r - \bar{a})/\bar{h}_a$: (a i) 10, (a ii) 11, (a iii) 12, (a iv) 8, (a v) 9, (a vi) 10, (a vii) 5, (a viii) 6 and (a ix) 7. (b) Here, $We = 22$, $St = 2.12 \times 10^4$ at τ values (b i–b iii) 12, (b iv–b vi) 15, (b vii–b ix) 20 and (b x–b xii) 40, for the following radial positions $(r - \bar{a})/\bar{h}_a$: (b i) 1, (b ii) 2, (b iii) 3, (b iv) 2, (b v) 3, (b vi) 4, (b vii) 1.5, (b viii) 2.5, (b ix) 3.5, (b x) 3.5, (b xi) 4.5 and (b xii) 5.5. (c) Here, $We = 48$, $St = 1.84 \times 10^4$ at τ values (c i–c iii) 12, (c iv–c vi) 15, (c vii–c ix) 20 and (c x–c xii) 40, for the following radial positions $(r - \bar{a})/\bar{h}_a$: (c i) 0.5, (c ii) 1, (c iii) 1.5, (c iv) 1, (c v) 1.5, (c vi) 2, (c vii) 2, (c viii) 2.5, (c ix) 3, (c x) 4, (c xi) 5 and (c xii) 5.5.

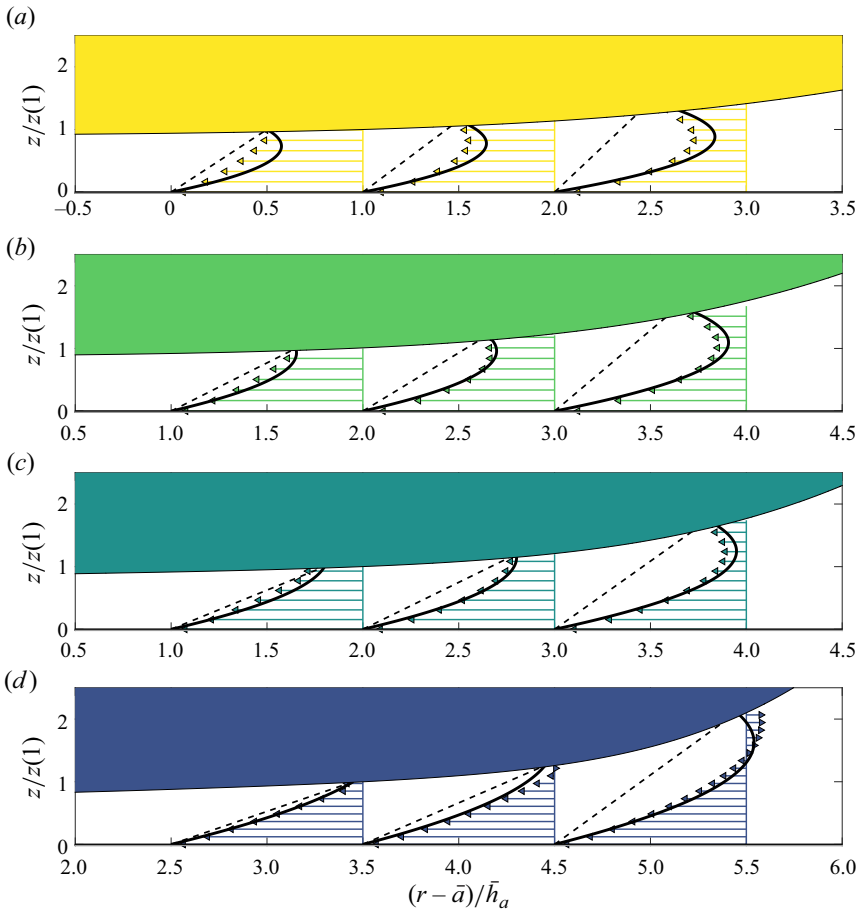


Figure 16. Comparison between u_r/V_m , with u_r indicating the radial component of the gas velocity field calculated numerically and V_m given in (3.3), with the prediction u_{th}/V_m corresponding to the capillary limit (χ_c) in (C4)–(C5). The velocity fields have been represented in the frame of reference moving with the wetting velocity V_m for four different instants of time τ , namely (a) 12, (b) 15, (c) 20 and (d) 40, and for three different values of $(r - \bar{a})/\bar{h}_a$, with $\bar{a} \approx R\sqrt{3}s$ and $\bar{h}_a \approx h_{a,m}$ given in (3.4). The velocity fields predicted by (C4)–(C5) are represented using black solid lines, whereas dashed lines illustrate the contribution of the Couette flow, corresponding to $\chi_c = 0$ in (C4). Here, $We = 22$, $St = 2.12 \times 10^4$, whereas $z(1)$ indicates the vertical coordinate of the interface at the minimum value of $(r - \bar{a})/\bar{h}_a$ represented in each of the plots.

We , St and τ are such that the impact takes place within the capillary regime described by the conditions given in (3.16)–(3.17), the interfacial liquid pressure along a distance $\ell_c > h_a$ located downstream the point of maximum pressure (see (3.7)–(3.8)) is larger than the atmospheric pressure, and in fact is comparable to the dynamic pressure. Then the capillary overpressures extending along a distance $\ell_c > h_a$ downstream of the point of maximum pressure contribute to decrease the value of the liquid tangential velocity at the interface with respect to Wagner’s expression for V_m . Hence the prediction for V_m could be improved by including in Wagner’s framework the contribution of the capillary normal stresses in the boundary condition for the potential at the interface along a region $\ell_c > h_a$ extending downstream of the point of maximum pressure. Here, ℓ_c (Gordillo & Riboux 2022) is a length that, when the impact takes place within the capillary regime defined in (3.16)–(3.17), is larger than the length h_a characterizing the so-called inner

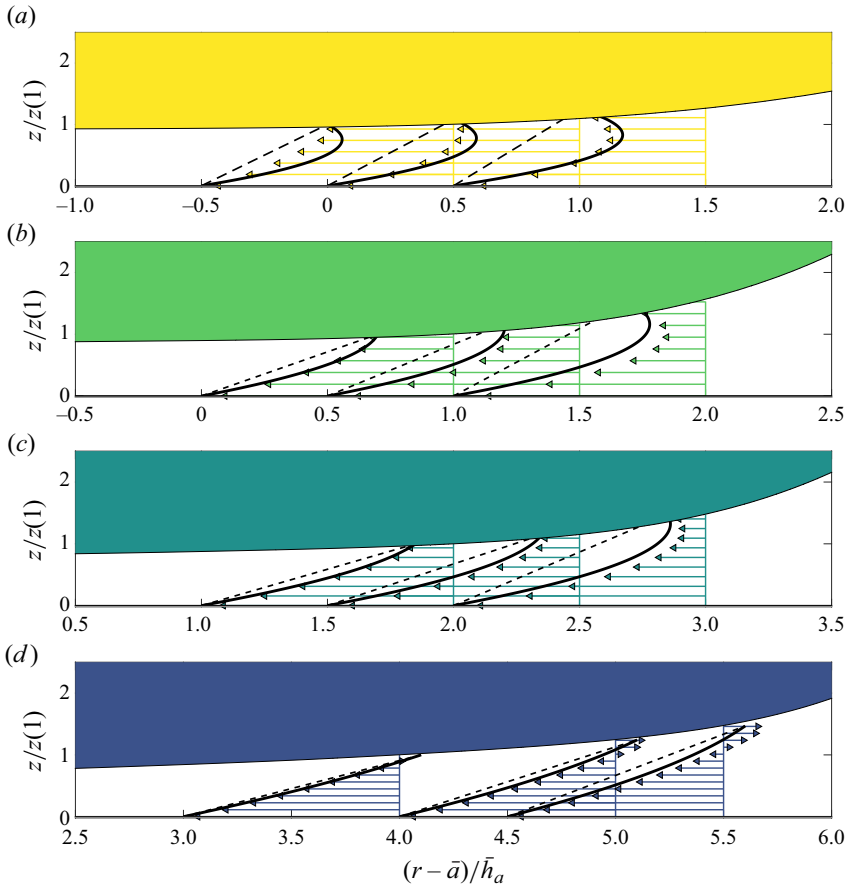


Figure 17. Comparison between u_r/V_m , with u_r indicating the radial component of the gas velocity field calculated numerically and V_m given in (3.3), with the prediction u_{th}/V_m corresponding to the inertial limit (χ_i) in (C4)–(C5). The velocity fields have been represented in the frame of reference moving with the wetting velocity V_m for four different instants of time τ , namely (a) 12, (b) 15, (c) 20 and (d) 40, and for three different values of $(r - \bar{a})/\bar{h}_a$, with $\bar{a} \approx R\sqrt{3}s$ and $\bar{h}_a \approx h_{a,m}$ given in (3.4). The velocity fields predicted by (C4)–(C5) are represented using black solid lines, whereas dashed lines illustrate the contribution of the Couette flow, corresponding to $\chi_i = 0$ in (C4). Here, $We = 48$, $St = 1.84 \times 10^4$, whereas $z(1)$ indicates the vertical coordinate of the interface at the minimum value of $(r - \bar{a})/\bar{h}_a$ represented in each of the figures.

solution in Wagner’s classical theory (Howison *et al.* 1991); this extra theoretical effort does not modify the essence of our physical modelling and could be considered in a separate contribution.

Figures 16 and 17 compare the gas velocity field calculated numerically for different instants of time in a frame of reference moving with velocity $V_m/U = 1/2\sqrt{3/s}$ along the spatial region where the maximum pressure is attained, with the velocity field resulting from the superposition of a parabolic Poiseuille flow plus a linear Couette flow given by the equation

$$\frac{u_{th}}{U}(r, s) = \frac{1}{2} \chi_{c,i} \left(\frac{St}{R^2} \right) [z(z - h(r, s))] + \frac{\sqrt{3}}{2} s^{-1/2} \left[K(s) \frac{z}{h(r, s)} - 1 \right], \quad (C4)$$

with $0.5 \leq K(s) \leq 1.1$ adjusted so that u_{th}/U in (C4) matches the value of the tangential velocity calculated numerically at $z = h(r, s)$. In (C4),

$$\left. \begin{aligned} \chi_c &= -A' \tau^{-11/6} We^{2/3} St^{14/9}, \\ \chi_i &= -B' \tau^{-5/2} St^{5/3}, \end{aligned} \right\} \quad (C5)$$

where we have made use of the results in (3.17), and $A' = 0.0114$ and $B' = 0.2449$ are the values of the proportionality constants deduced from figure 14. The results in figures 16 and 17 show that the interfacial velocity in the moving frame of reference is not zero; this would be the case only if $K(s) = 1$ in (C4). Nevertheless, these deviations cannot be attributed to the shear stresses exerted by the gas at the interface; indeed, the gas shear stresses would induce a liquid interfacial velocity that, in the moving frame of reference, would point in the direction opposite to that shown in figures 16 and 17, and, moreover, as can be seen clearly in figure 15, the gradients of the radial liquid velocity along the vertical coordinate are fairly small as a consequence of the smallness of the gas to liquid viscosity ratio; see (C1). Then the reason for $K \neq 1$ in (C4) is associated with the simplifications made in the potential flow description since, as was indicated previously, Wagner's theory does not take into account the effect of the capillary pressure and the actual geometry of the bottom part of the drop has been linearized; indeed, notice that the boundary conditions corresponding to the solutions of the Laplace equation used here have been imposed at $z = 0$; see Gordillo & Riboux (2022) for details.

REFERENCES

- BOUWHUIS, W., VAN DER VEEN, R.C.A., TRAN, T., KEIJ, D.L., WINKELS, K.G., PETERS, I.R., VAN DER MEER, D., SUN, C., SNOEIJER, J.H. & LOHSE, D. 2012 Maximal air bubble entrainment at liquid-drop impact. *Phys. Rev. Lett.* **109**, 264501.
- CHANDRA, S. & AVEDISIAN, C.T. 1991 On the collision of a droplet with a solid surface. *Proc. R. Soc. Lond. A* **432** (1884), 13–41.
- CHANTELOT, P. & LOHSE, D. 2021 Drop impact on superheated surfaces: short-time dynamics and transition to contact. *J. Fluid Mech.* **928**, A36.
- CHANTELOT, P. & LOHSE, D. 2023 Drop impact on superheated surfaces: from capillary dominance to non-linear advection dominance. *J. Fluid Mech.* **963**, A2.
- CHUBYNSKY, M.V., BELOUSOV, K.I., LOCKERBY, D.A. & SPRITTLES, J.E. 2020 Bouncing off the walls: the influence of gas-kinetic and van der Waals effects in drop impact. *Phys. Rev. Lett.* **124**, 084501.
- DUCHEMIN, L. & JOSSEAND, C. 2011 Curvature singularity and film-skating during drop impact. *Phys. Fluids* **23** (9), 091701.
- DUCHEMIN, L. & JOSSEAND, C. 2012 Rarefied gas correction for the bubble entrapment singularity in drop impacts. *C. R. Méc.* **340** (11), 797–803.
- DE GOEDE, T.C., DE BRUIN, K.G., SHAHIDZADEH, N. & BONN, D. 2019 Predicting the maximum spreading of a liquid drop impacting on a solid surface: effect of surface tension and entrapped air layer. *Phys. Rev. Fluids* **4**, 053602.
- GORDILLO, J.M. & RIBOUX, G. 2022 The initial impact of drops cushioned by an air or vapour layer with applications to the dynamic Leidenfrost regime. *J. Fluid Mech.* **941**, A10.
- HICKS, P.D. & PURVIS, R. 2010 Air cushioning and bubble entrapment in three-dimensional droplet impacts. *J. Fluid Mech.* **649**, 135–163.
- HOWISON, S.D., OCKENDON, J.R. & WILSON, S.K. 1991 Incompressible water-entry problems at small deadrise angles. *J. Fluid Mech.* **222**, 215–230.
- JOSSEAND, C. & THORODDSEN, S.T. 2016 Drop impact on a solid surface. *Annu. Rev. Fluid Mech.* **48** (1), 365–391.
- KIM, H., TRUONG, B., BUONGIORNO, J. & HU, L.-W. 2011 On the effect of surface roughness height, wettability, and nanoporosity on Leidenfrost phenomena. *Appl. Phys. Lett.* **98** (8), 083121.
- KOLINSKI, J.M., MAHADEVAN, L. & RUBINSTEIN, S.M. 2014a Drops can bounce from perfectly hydrophilic surfaces. *Europhys. Lett.* **108** (2), 24001.

- KOLINSKI, J.M., MAHADEVAN, L. & RUBINSTEIN, S.M. 2014*b* Lift-off instability during the impact of a drop on a solid surface. *Phys. Rev. Lett.* **112** (13), 134501.
- KOROBKIN, A.A., ELLIS, A.S. & SMITH, F.T. 2008 Trapping of air in impact between a body and shallow water. *J. Fluid Mech.* **611**, 365–394.
- KOROBKIN, A.A. & PUKHNACHOV, V.V. 1988 Initial stage of water impact. *Annu. Rev. Fluid Mech.* **20** (1), 159–185.
- KOROBKIN, A.A. & SCOLAN, Y.-M. 2006 Three-dimensional theory of water impact. Part 2. Linearized Wagner problem. *J. Fluid Mech.* **549**, 343–373.
- LI, J. 2016 Macroscopic model for head-on binary droplet collisions in a gaseous medium. *Phys. Rev. Lett.* **117**, 214502.
- VAN LIMBEEK, M.A.J., HOEFNAGELS, P.B.J., SUN, C. & LOHSE, D. 2017 Origin of spray formation during impact on heated surfaces. *Soft Matt.* **13**, 7514–7520.
- MANDRE, S. & BRENNER, M.P. 2012 The mechanism of a splash on a dry solid surface. *J. Fluid Mech.* **690**, 148–172.
- MANDRE, S., MANI, M. & BRENNER, M.P. 2009 Precursors to splashing of liquid droplets on a solid surface. *Phys. Rev. Lett.* **102**, 134502.
- MANI, M., MANDRE, S. & BRENNER, M.P. 2010 Events before droplet splashing on a solid surface. *J. Fluid Mech.* **647** (1), 163–185.
- MISHRA, S., RUBINSTEIN, S.M. & RYCROFT, C.H. 2022 Computing the viscous effect in early-time drop impact dynamics. *J. Fluid Mech.* **945**, A13.
- MOORE, M.R. 2014 New mathematical models for splash dynamics. PhD thesis, Oxford University.
- MOORE, M.R. 2021 Introducing pre-impact air-cushioning effects into the Wagner model of impact theory. *J. Engng Maths* **129**, 6.
- OLIVER, J.M. 2002 Water entry and related problem. PhD thesis, Oxford University.
- PETERS, I.R., VAN DER MEER, D. & GORDILLO, J.M. 2013 Splash wave and crown breakup after disc impact on a liquid surface. *J. Fluid Mech.* **724**, 553–580.
- POPINET, S. 2015 A quadtree-adaptive multigrid solver for the Serre–Green–Naghdi equations. *J. Comput. Phys.* **302**, 336–358.
- RIBOUX, G. & GORDILLO, J.M. 2014 Experiments of drops impacting a smooth solid surface: a model of the critical impact speed for drop splashing. *Phys. Rev. Lett.* **113**, 024507.
- ROSS, S. & HICKS, P.D. 2019 A comparison of pre-impact gas cushioning and Wagner theory for liquid–solid impacts. *Phys. Fluids* **31** (4), 042101.
- DE RUITER, J., OH, J.M., VAN DEN ENDE, D. & MUGELE, F. 2012 Dynamics of collapse of air films in drop impact. *Phys. Rev. Lett.* **108**, 074505.
- SANJAY, V. 2022 Code repository. <https://github.com/VatsalSy/Impact-forces-of-water-drops-falling-on-superhydrophobic-surfaces>.
- SCOLAN, Y. & KOROBKIN, A. 2001 Three-dimensional theory of water impact. Part 1. Inverse Wagner problem. *J. Fluid Mech.* **440**, 293–326.
- SHARIPOV, F., CUMIN, L.M.G. & KALEMPA, D. 2007 Heat flux between parallel plates through a binary gaseous mixture over the whole range of the Knudsen number. *Physica A* **378** (2), 183–193.
- SHIROTA, M., VAN LIMBEEK, M.A.J., SUN, C., PROSPERETTI, A. & LOHSE, D. 2016 Dynamic Leidenfrost effect: relevant time and length scales. *Phys. Rev. Lett.* **116**, 064501.
- SMITH, F.T., LI, L. & WU, G.X. 2003 Air cushioning with a lubrication/inviscid balance. *J. Fluid Mech.* **482**, 291–318.
- SOBAC, B., REDNIKOV, A., DORBOLO, S. & COLINET, P. 2014 Leidenfrost effect: accurate drop shape modeling and refined scaling laws. *Phys. Rev. E* **90**, 053011.
- SPRITTLES, J.E. 2024 Gas microfilms in droplet dynamics: when do drops bounce? *Annu. Rev. Fluid Mech.* **56** (1), 91–118.
- THORODDSEN, S.T., ETOH, T.G., TAKEHARA, K., OOTSUKA, N. & HATSUKI, Y. 2005 The air bubble entrapped under a drop impacting on a solid surface. *J. Fluid Mech.* **545**, 203–212.
- TRAN, T., STAAT, H.J.J., PROSPERETTI, A., SUN, C. & LOHSE, D. 2012 Drop impact on superheated surfaces. *Phys. Rev. Lett.* **108**, 036101.
- TRAN, T., STAAT, H.J.J., SUSARREY-ARCE, A., FOERTSCH, T.C., VAN HOUSELT, A., GARDENIERS, H.J.G.E., PROSPERETTI, A., LOHSE, D. & SUN, C.AO 2013 Droplet impact on superheated micro-structured surfaces. *Soft Matt.* **9**, 3272–3282.
- WAGNER, H. 1932 Über stoß- und gleitvorgänge an der oberfläche von flüssigkeiten. *Z. Angew. Math. Mech.* **12** (4), 193–215.
- WILSON, S.K. 1989 The mathematics of ship slamming. PhD thesis, Oxford University.

- ZHANG, B., SANJAY, V., SHI, S., ZHAO, Y., LV, C., FENG, X.-Q. & LOHSE, D. 2022 Impact forces of water drops falling on superhydrophobic surfaces. *Phys. Rev. Lett.* **129**, 104501.
- ZHANG, P. & LAW, C.K. 2011 An analysis of head-on droplet collision with large deformation in gaseous medium. *Phys. Fluids* **23** (4), 042102.